

Published in final edited form as:

*Neuroimage*. 2014 April 1; 89: 92–109. doi:10.1016/j.neuroimage.2013.12.007.

## Whole brain mapping of water pools and molecular dynamics with rotating frame MR relaxation using gradient modulated low-power adiabatic pulses

Ovidiu C. Andronesi<sup>1,\*,#</sup>, Himanshu Bhat<sup>2</sup>, Martin Reuter<sup>3</sup>, Shreya Mukherjee<sup>1</sup>, Peter Caravan<sup>1</sup>, and Bruce R. Rosen<sup>1</sup>

<sup>1</sup>Athinoula A. Martinos Center for Biomedical Imaging, Department of Radiology, Massachusetts General Hospital, Harvard Medical School, Boston, MA 02114

<sup>2</sup>Siemens Medical Solutions USA Inc, Charlestown, MA 02129

<sup>1</sup>Athinoula A. Martinos Center for Biomedical Imaging, Department of Neurology, Massachusetts General Hospital, Harvard Medical School, Boston, MA 02114

### Abstract

Nuclear magnetic resonance (NMR) relaxation in the rotating frame is sensitive to molecular dynamics on the time scale of water molecules interacting with macromolecules or supramolecular complexes, such as proteins, myelin and cell membranes. Hence, longitudinal ( $T1\rho$ ) and transverse ( $T2\rho$ ) relaxation in the rotating frame may have a great potential to probe the macromolecular fraction of tissues. This stimulated a large interest in using this MR contrast to image brain under healthy and disease conditions. However, experimental challenges related to the use of intense radiofrequency irradiation have limited the widespread use of  $T1\rho$  and  $T2\rho$  imaging. Here, we present methodological development to acquire 3D high-resolution or 2D (multi-)slice selective  $T1\rho$  and  $T2\rho$  maps of the entire human brain within short acquisition times. These improvements are based on a class of gradient modulated adiabatic pulses that reduce the power deposition, provide slice selection, and mitigate artifacts resulting from inhomogeneities of  $B_1$  and  $B_0$  magnetic fields. Based on an analytical model of the  $T1\rho$  and  $T2\rho$  relaxation we compute the maps of macromolecular bound water fraction, correlation and exchange time constants as quantitative biomarkers informative of tissue macromolecular content. Results obtained from simulations, phantoms and five healthy subjects are included.

### Keywords

Rotating frame relaxation ( $T1\rho$ ,  $T2\rho$ ); Macromolecular content; Correlation time; Exchange time; Bound water fraction; Neurodegeneration

---

<sup>#</sup>Presented in part at the 21<sup>st</sup> Annual Meeting of ISMRM, Salt Lake City, UT, 20–26 Apr, 2013.

© 2013 Elsevier Inc. All rights reserved.

\*Address correspondence/reprints request to: Ovidiu C. Andronesi, Athinoula A. Martinos Center for Biomedical Imaging, Massachusetts General Hospital, Harvard Medical School, 149 Thirteenth Street, Suite 2301, Charlestown, MA 02129, USA; ovidiu@nmr.mgh.harvard.edu, Tel: 617-643-6864; Fax: 617 726-7422.

**Publisher's Disclaimer:** This is a PDF file of an unedited manuscript that has been accepted for publication. As a service to our customers we are providing this early version of the manuscript. The manuscript will undergo copyediting, typesetting, and review of the resulting proof before it is published in its final citable form. Please note that during the production process errors may be discovered which could affect the content, and all legal disclaimers that apply to the journal pertain.

## 1. INTRODUCTION

Longitudinal ( $T1\rho$ ) and transverse ( $T2\rho$ ) relaxation in the rotating frame of nuclear magnetic resonance can probe water molecules loosely bound (hydration layer) to macromolecules. The macromolecular fraction is tissue specific and changes with disease, hence  $T1\rho$  and  $T2\rho$  have been proposed (Sepponen et al., 1985) as a candidate for non-invasive imaging solid tissue matrix, albeit indirectly through the relaxation of water interacting with macromolecules. Several studies have investigated the value of  $T1\rho$  and  $T2\rho$  imaging in the context of neurological diseases, including Alzheimer's Disease (Borthakur et al., 2008, Haris et al., 2011), Parkinson Disease (Michaeli et al., 2007, Haris et al., 2011), stroke (Jokivarsi et al., 2009, Jokivarsi et al., 2010a), and brain cancer (Aronen et al., 1999, Hakumaki et al., 1999). These studies revealed that  $T1\rho$  and  $T2\rho$  relaxation times have a broader range of values compared to  $T1$  and  $T2$  across disease spectrum, and better separate patients from controls. Also,  $T1\rho$  and  $T2\rho$  relaxation times seem to correlate better and earlier with therapy response or disease progression when compared to other MRI markers such as laboratory frame  $T1$  and  $T2$  relaxation, or ADC values (Duvvuri et al., 2001, Hakumaki et al., 2002, Jokivarsi et al., 2010a).

Experimental challenges related to high specific absorption rate (SAR), non-selective spatial excitation, long acquisition times, and artifacts from  $B_0$  and  $B_1$  inhomogeneity currently prevent a wide spread adoption and usage of  $T1\rho$  and  $T2\rho$  in the neuroimaging community. Here, we present methodological development for clinically feasible and robust  $T1\rho$  and  $T2\rho$  mapping of the whole human brain based on a recent class of gradient modulated adiabatic pulses (Andronesi et al., 2010). Further, using an analytical model and fitting of relaxation curves we extract tissue specific maps for parameters of molecular dynamics such as correlation times, exchange times, and water pools.

Nuclear spin relaxation in the rotating frame is obtained when a radiofrequency field ( $B_1$ ) is applied either along or perpendicular to the nuclear magnetization for longitudinal  $T1\rho$  relaxation or transverse  $T2\rho$  relaxation, respectively. Typically,  $T1\rho$  and  $T2\rho$  imaging of the human brain is done with  $B_1$  amplitudes in the range of 0.5–1 kHz and durations between 50–100 ms. The combination of high  $B_1$  amplitude and long duration leads to increased SAR, which is often circumvented by increasing repetition times (TR) leading to long acquisition times (TA). Moreover, in all imaging studies so far  $T1\rho$  and  $T2\rho$  relaxation has been achieved via spatially non-selective radiofrequency (RF) irradiation, which further imposes limits on the TR in multislice experiments due to relaxation and saturation of magnetization in neighboring slices. As a result, rotating frame relaxation imaging is usually performed as a single slice or very few (1–4) slices at a time.

Three main approaches are currently used to achieve  $T1\rho$  relaxation: i) the on-resonance continuous wave (CW) method where the magnetization is first flipped in the transverse plane and a  $B_1$  field with a constant amplitude is applied along magnetization for spin-lock (Aronen et al., 1999), ii) the off-resonance continuous wave (CW) method where an offset is used to create an effective field and magnetization is flipped along the direction of the effective field (Ramadan et al., 1998), and iii) a train of adiabatic inversion pulses producing repeated passages of the longitudinal magnetization between the +Z and -Z orientations via amplitude and frequency modulation of  $B_1$  field (Michaeli et al., 2008). In the case of  $T2\rho$  relaxation the initial magnetization is first flipped perpendicular to the direction of the spin-lock or the effective field for precession around it. The spin-lock method is easier to implement and model analytically, but it is more sensitive to artifacts induced by  $B_0$  and  $B_1$  inhomogeneities. These artifacts can be compensated over a reduced  $B_0$  and  $B_1$  range by composite pulses and phase alternation of the CW spin-lock (Witschey et al., 2007). On the other hand, due to its simultaneous frequency and amplitude sweep adiabatic pulses can

cover a much larger bandwidth of  $B_0$  offsets and can tolerate several-folds of  $B_1$  inhomogeneity above the adiabatic threshold (Garwood and DelaBarre, 2001). In addition, adiabatic pulses have lower SAR compared to a CW spin-lock of the same amplitude.

Our focus in this work was to address the major limitations of current T1 $\rho$  and T2 $\rho$  imaging techniques, namely high SAR and long acquisition times, while at the same time compensating for  $B_0$  and  $B_1$  inhomogeneities. Gradient modulated adiabatic pulses such as GOIA-W(16,4) (Andronesi et al., 2010) simultaneously meet all these requirements. The Gradient Offset Independent Adiabaticity (GOIA) design (Tannus and Garwood, 1997) lowers the maximum  $B_1$  amplitude by 55%, resulting in 80% less SAR, compared to conventional adiabatic pulses of the same bandwidth and duration. Alternatively, GOIA-W(16,4) can be made shorter and still have lower  $B_1$  amplitude than conventional adiabatic pulses, allowing more flexibility in choosing the duration of T1 $\rho$  and T2 $\rho$  preparation. Compared to a CW spin-lock of the same amplitude GOIA-W(16,4) pulses would have 20% less SAR.

The use of gradient modulation in GOIA-W(16,4) pulses naturally provides slice-selectivity for T1 $\rho$  and T2 $\rho$ . In the case of 2D imaging, slice selectivity allows the use of a short TR to acquire a stack of slices without saturating magnetization of neighboring slices. Although strategies have been proposed for the CW spin-lock method to reduce SAR (Wheaton et al., 2004a) or acquire multiple slices with less magnetization saturation (Wheaton et al., 2004b), these have limitations in fully achieving those goals. In terms of the SAR deposition, GOIA pulses compare favorably also to relaxation along the fictitious field (RAFF) method (Liimatainen et al., 2010) which uses sub-adiabatic RF frequency and amplitude modulations to lower  $B_1$  requirements, at the cost of more sensitivity to  $B_1$  inhomogeneity and without slice selectivity.

Here we demonstrate the use of GOIA-W(16,4) pulses trains in combination with 2D spin-echo EPI (EPI-SE) and 3D turbo FLASH (TFL) readouts as a new method for robust and feasible T1 $\rho$  and T2 $\rho$  imaging of the human brain.

## 2. THEORY

### 2.1 Relaxation in the rotating frame of GOIA pulses

Relaxation in the rotating frame has been an important research topic reach in applications since the beginning of nuclear magnetic resonance (Redfield, 1957). The semi-classical theory of Bloch-Wangsness-Redfield (BWR), often used for practical reasons, treats the spins quantum mechanically and the lattice as random perturbation described by classical statistics (Wangsness and Bloch, 1953, Redfield, 1957, Abragam, 1961). Significant progress has been made over the last decade in laying out the analytical framework for relaxation in the rotating frame under adiabatic pulses (Sorce et al., 2007, Michaeli et al., 2008, Mangia et al., 2009). In this work we extend the theory of rotating frame relaxation for the case of gradient modulated adiabatic pulses.

GOIA pulses (Tannus and Garwood, 1997) are obtained by simultaneously modulating the amplitude  $B_1(t)$  and frequency  $\Delta\omega(t)$  of RF field, together with the slice selection gradient  $G(t)$  according to:

$$\Delta\omega(t) = \frac{1}{Q} G(t) \int_0^t \frac{\gamma^2 B_1^2(t')}{G(t')} dt' \quad [1]$$

where  $Q$  is the adiabatic factor, and  $\gamma$  is the nuclear gyromagnetic ratio.

In particular, for GOIA-W(16,4) pulses (Andronesi et al., 2010) the modulation functions  $B_1(t)$  and  $G(t)$  are based on the wideband uniform rate and smooth truncation WURST (Kupce and Freeman, 1995) function:

$$B_1(t) = B_{1,max} \left( 1 - [\sin(\pi/2(2t/T_p - 1))]^{16} \right) \quad G(t) = G_{max} \left( (1 - g_m) + g_m [\sin(\pi/2(2t/T_p - 1))]^4 \right) \quad [2]$$

where  $T_p$  is the pulse duration,  $B_{1,max}$  is the maximum RF amplitude,  $G_{max}$  is the maximum gradient, and  $g_m \in [0, 1]$  is the gradient modulation factor. The larger the  $g_m$  factor the more the gradient drops in the middle of the pulse and correspondingly lesser RF amplitude is required, an effect also known as the variable rate selective excitation VERSE (Conolly et al., 1988). Alternatively, GOIA-HS(8,4) (Andronesi et al., 2010) pulses are obtained if stretched hyperbolic-secant functions are used instead of WURST. Besides pulse duration and gradient modulation factor, the exponents of trigonometric functions can be varied too, providing great flexibility in obtaining new pulses. Modulations of GOIA-W(16,4) pulse of 4ms duration and 5kHz bandwidth are shown in Figs. 1A–C.

In order to calculate the rates of rotating frame relaxation we need the effective field ( $\omega_{eff}$ ) and the magnetization nutation angle ( $\alpha$ ):

$$\omega_{eff}(t, x) = \sqrt{(\gamma B_1(t))^2 + ((\Delta\omega(t) + \gamma x G(t)))^2} \quad \alpha(t, x) = \text{atan}(\gamma B_1(t) / (\Delta\omega(t) + \gamma x G(t))) \quad [3]$$

The adiabatic condition states that the effective field should be much greater than the rate nutation angle  $\omega_{eff}(t, x) \gg \alpha(t, x)$  at all times and positions. In practice an adiabatic factor  $Q = \omega_{eff}/\alpha > 5$  and a time-bandwidth product  $R > 20$  are needed to have an adiabatic pulse. Plots of the effective field modulation, nutation angle and inverse of adiabatic factor during the GOIA-W(16,4) pulse are shown in Figs. 1D–F. The adiabatic factor is greater than 5 for the most part of the pulse with the exception of short periods in the vicinity of 1.2ms and 2.8ms where it decreases to 3. By increasing the R product the pulse becomes more adiabatic.

An important observation is necessary at this point. Due to gradient modulation the effective field and nutation angle in Eqs. [3] become dependent on the spatial coordinate  $x$  in the slice direction. However, there is dependency only of the intra-slice isochromats, and not of the slice position relative to the isocenter. The effect of slice position is cancelled by the additional frequency modulation that is used to excite slices off-isocenter. For simplicity this term was not included in Eq. [1], but more details are given in (Andronesi et al., 2010). Thus, the slices at isocenter and off-isocenter positions have the same effective field and nutation angle, and consequently the relaxation rate does not depend on the slice position. As we will show next, what is relevant for the measurement is the average relaxation rate over the pulse duration and slice thickness, which can be exactly calculated.

A physical model that satisfactorily approximates the rotating frame relaxation of water in vivo includes two main relaxation mechanisms: dipolar coupling and exchange interactions (Michaeli et al., 2004, Michaeli et al., 2005, Sorce et al., 2007, Michaeli et al., 2008). Random fluctuations due to reorientation of the direct proton-proton dipolar coupling and exchange of protons between sites with different chemical shifts or diffusion through microscopic field inhomogeneities lead to decoherence of the spin system. The stochastic nature of random perturbations is described by the spectral density functions of the type ( $n = 0, 1, 2$ ):

$$J_n(\tau) \sim \tau / (1 + (n\omega\tau)^2) \quad [4]$$

where  $\tau$  may represent the correlation time  $\tau_c$  or exchange time  $\tau_{ex}$ , and  $\omega$  may represent the Larmor frequency  $\omega_0 = \gamma B_0$  or the effective field  $\omega_{eff}$  from Eq. [3]. The most commonly employed model (Michaeli et al., 2008, Sierra et al., 2008, Jokivarsi et al., 2009, Mangia et al., 2009) for deriving rotating frame relaxation in tissues assumes a two sites exchange model (2SX) at equilibrium between the free water (slow relaxing component) and the water bound to macromolecules (fast relaxing component), as shown schematically in Figure 2.

Relaxation rates in the rotating frame (Blicharski, 1972) can be cast in a time dependent form for adiabatic pulses as instantaneous relaxation rates (Michaeli et al., 2008, Mangia et al., 2009). In the case of GOIA-W(16,4) pulses the instantaneous relaxation rate for dipolar coupling interaction becomes dependent on the intra-slice isochromat at position  $x$

$$R_{1\rho}^{dd}(t, x) = \frac{D_c}{10} \tau_c \times \left[ \frac{3\sin^2\alpha(t, x)\cos^2\alpha(t, x)}{1+(\omega_{eff}(t, x)\tau_c)^2} + \frac{3\sin^4\alpha(t, x)}{1+(2\omega_{eff}(t, x)\tau_c)^2} + \frac{2+3\sin^2\alpha(t, x)}{1+(\omega_0\tau_c)^2} + \frac{8-6\sin^2\alpha(t, x)}{1+(2\omega_0\tau_c)^2} \right] \quad [5]$$

$$R_{2\rho}^{dd}(t, x) = \frac{D_c}{40} \tau_c \times \left[ 3(3\cos^2\alpha(t, x) - 1)^2 + \frac{30\sin^2\alpha(t, x)\cos^2\alpha(t, x)}{1+(\omega_{eff}(t, x)\tau_c)^2} + \frac{3\sin^4\alpha(t, x)}{1+(2\omega_{eff}(t, x)\tau_c)^2} + \frac{20-6\sin^2\alpha(t, x)}{1+(\omega_0\tau_c)^2} + \frac{8+12\sin^2\alpha(t, x)}{1+(2\omega_0\tau_c)^2} \right]$$

where the dipolar coupling constant  $D_c = 2I(I+1)[\mu_0 \hbar \gamma^2 / (4\pi r^3)]^2$ ,  $I = 1/2$  is the spin number, and the physical constants are  $\mu_0 = 4\pi \cdot 10^{-7}$  H/m the vacuum magnetic permeability,  $\hbar = 1.055 \cdot 10^{-34}$  Js the Planck's constant,  $\gamma = 2\pi \cdot 42.576 \cdot 10^6$  rad/(sT) the gyromagnetic ratio, and  $r = 1.58 \text{ \AA}$  is the proton-proton distance in water molecule. Simulations of dipolar relaxation rates for GOIA-W(16,4) pulses are shown in Figure 3(A,C).

Similarly, the instantaneous relaxation rates for the anisochronous exchange interaction can be obtained in the form of

$$R_{1\rho}^{ex}(t, x) = P_b P_f (\delta\omega_{ex})^2 \tau_{ex} \frac{\sin^2\alpha(t, x)}{1+(\omega_{eff}(t, x)\tau_{ex})^2} \quad R_{2\rho}^{ex}(t, x) = P_b P_f (\delta\omega_{ex})^2 \tau_{ex} \cos^2\alpha(t, x) \quad [6]$$

where  $P_b$  is the pool of bound water,  $P_f$  is the pool of free water ( $P_b + P_f = 1$ ), and  $\delta\omega_{ex}$  is the chemical shift difference between the two exchanging sites. Simulations for exchange relaxation rates during GOIA-W(16,4) pulses are presented in Figure 3B,D.

The intrinsic instantaneous relaxations rates Eqs. [5–6] are further used to compute the observed relaxation rates. First, the average dipolar and exchange relaxation rates over pulse duration need to be calculated for each slice isochromat:

$$\overline{R_{1\rho,2\rho;b,f}^{dd,ex}}(x) = \frac{1}{T_p} \int_0^{T_p} R_{1\rho,2\rho;b,f}^{dd,ex}(t, x) dt \quad [7]$$

For each isochromat we can then calculate the observed (or apparent) relaxation rate averaged over the pulse duration. Under in-vivo conditions the fast exchange limit  $\delta\omega_{ex}\tau_{ex} \ll 1$  (FXL) is assumed (Sierra et al., 2008, Jokivarsi et al., 2009), and the observed relaxation rate is obtained as a linear combination between dipolar relaxation of free and bound water, and exchange relaxation:

$$\overline{R_{1\rho,2\rho}^{obs}}(x) = P_b(x)\overline{R_{1\rho,2\rho;b}^{dd}}(x) + P_f(x)\overline{R_{1\rho,2\rho;f}^{dd}}(x) + \overline{R_{1\rho,2\rho}^{ex}}(x) \quad [8]$$

By integrating the exponential decays of all isochromats over the slice thickness we can obtain the time-spatial average of the observed relaxation rate:

$$\overline{R_{1\rho,2\rho}^{obs}} = -\frac{1}{T_p} \ln \left[ \frac{1}{\Delta x \overline{S_0}} \int_{-\Delta x/2}^{\Delta x/2} S_0(x) \exp(-\overline{R_{1\rho,2\rho}^{obs}}(x) \cdot T_p) dx \right] \quad [9]$$

where the mean initial magnetization (signal) over the slice is  $\overline{S_0} = 1/\Delta x \int_{-\Delta x/2}^{\Delta x/2} S_0(x) dx$ . Note that under the most general conditions the correlation times, exchange times, exchange rate, water pools and initial signal can vary spatially across isochromats. In certain conditions, such as activation, the model parameters could vary also on the time scale of the pulse. This variation is captured implicitly in the Eqs. [6–9]. Simulations for the average observed relaxation rates during GOIA-W(16,4) pulses are presented in Figure 4 as a function of model parameters.

In the case when the change in the relaxation rates and initial signal is small among isochromats Eqs. [7–9] may be linearized and the average relaxations can be very well approximated by:

$$\overline{R_{1\rho,2\rho;b,f}^{dd,ex}} = \frac{1}{T_p} \frac{1}{\Delta x} \int_{-\Delta x/2}^{\Delta x/2} \int_0^{T_p} R_{1\rho,2\rho;b,f}^{dd,ex}(t, x) dt dx \quad \overline{R_{1\rho,2\rho}^{obs}} = P_b \overline{R_{1\rho,2\rho;b}^{dd}} + P_f \overline{R_{1\rho,2\rho;f}^{dd}} + \overline{R_{1\rho,2\rho}^{ex}} \quad [10]$$

Simulations performed in Figure 5C–F show the results for the average observed relaxation rates obtained from Eqs. [7–9] or Eqs. [10].

The 2SX/FXL model depicted in Figure 2 is described by a maximum number of seven independent parameters: two correlation times (for bound and free water), two proton-proton distances (for bound and free water), population of bound site ( $P_f = 1 - P_b$ ), exchange time, and chemical shift difference. However, three parameters can be readily eliminated considering the same proton-proton distance (1.58 Å) for both bound and free water, and a standard value for the correlation time of free water (5 ps). In this case the observed relaxation rate is determined by the four remaining parameters: the correlation time of bound water, exchange time, chemical shift difference, and the population of bound water. In the ideal situation of no measurement noise a minimum number of four experimental time points are necessary to obtain the molecular parameters of interest, however experimentally extra time points are beneficial. Figure 4 shows simulations of the observed rotating frame relaxation rate under GOIA-W(16,4) pulses for relevant in-vivo model parameters.

## 2.2 Diffusion weighting during rotating frame relaxation under GOIA pulses

The use of the gradient modulation during relaxation in the rotating frame of GOIA pulses raises the question of what is the effect of diffusion on the signal decay. The effect of diffusion may be expected particularly for T2ρ where magnetization precesses around the effective field and diffusion may produce signal decay similarly like in spin echo experiments. In the case of T1ρ magnetization spends most of the time longitudinally and there is no evolution of the spin echo type.

A few papers have investigated the effects of diffusion during adiabatic pulses in spin echo experiments (Sun and Bartha, 2007, Valette et al., 2010). In deriving an expression for the b-

value produced by the T2ρ preparation with GOIA-W(16,4) pulses we will follow the approach proposed in (Valette et al., 2010). Most generally, the b-value associated with a gradient  $G(t)$  is obtained as the integral of the square of the gradient moment  $k(t)$

$$b(t) = \int_0^t k^2(t') dt' \quad \text{where } k(t') = \gamma \int_0^{t'} G(t'') dt'' \quad [11]$$

To calculate the gradient moment for the GOIA-W(16,4) pulse we can use the commonly assumed approximation (Pipe, 1995, Park and Garwood, 2009) that for a given isochromat located at position  $x$  within the slice ( $-\Delta x/2 \leq x \leq \Delta x/2$ ) the magnetization is flipped instantaneously when  $\Delta\omega(t_x) = \gamma x G(t_x)$ . Under this assumption, it has been shown (Valette et al., 2010) that during adiabatic frequency-swept pulses the only contribution to diffusion weighting comes from the phase scrambling due to gradient, while the scrambling effect due to the quadratic phase induced by the frequency modulation of the  $B_1$  field cancels out. The 180° flip of magnetization will change the sign of the gradient moment at the instant time  $t_x$

$$k(t', x) = \begin{cases} \gamma \int_0^{t'} G(t'') dt'', & 0 \leq t' \leq t_x \\ \gamma \int_0^{t'} G(t'') dt'' - 2 \cdot \gamma \int_0^{t_x} G(t'') dt'', & t_x < t' \leq T_p \end{cases} \quad [12]$$

where the flipping time  $t_x \in [0, T_p]$  is given by the solution of

$$\gamma \int_0^{t_x} B_1^2(t) / G(t) dt = Qx \quad [13]$$

with  $B_1(t)$  and  $G(t)$  defined by Eqs. [2]. While solving Eq. [11] by integration of  $B_1(t)$  and  $G(t)$  modulations given in Eqs. [2] leads to a very complicated analytical solution, it can be shown that the inversion time for each isochromat can be simply calculated from:

$$t_x = \frac{T_p}{2} \left( 1 + \frac{2x \cdot G(t)}{\Delta x \cdot G_{max}} \right), \quad x \in \left[ -\frac{\Delta x}{2}, \frac{\Delta x}{2} \right] \quad [14]$$

This can be verified also numerically by simulations of the slice profile during the pulse as shown in Figure 5A. Plots of the inversion times and gradient moment are shown in Figs. 5B and 5G, respectively.

From Eqs. [12–14] it can be seen that the gradient moment and b-value become dependent on the isochromat position. Considering a pair of two GOIA-W(16,4) pulses as the diffusion weighting element the spatial dependent b-value can be calculated:

$$b(x) = \int_0^{2T_p} k^2(t, x) dt \quad [15]$$

Simulation of the b-values across the slice profile for a pair of GOIA-W(16,4) pulses is shown in Fig. 5H. An average b-value for the entire slice can be calculated similarly like in the relaxation case:

$$\bar{b} = -\frac{1}{\bar{D}} \ln \left[ \frac{1}{\Delta x \bar{S}_0} \int_{-\Delta x/2}^{\Delta x/2} S_0(x) \exp(-b(x) \cdot D(x)) dx \right] \quad [16]$$

where  $D(x)$  is the diffusion coefficient, which most generally may vary across slice, and the mean coefficient  $\bar{D} = 1/\Delta x \cdot \int_{-\Delta x/2}^{\Delta x/2} D(x) dx$ , and  $\bar{S}_0$  is defined similarly like in the case of relaxation. In the case there is small change in b-value  $b(x)$ , diffusion coefficient  $D(x)$  and initial signal  $S_0(x)$  across the slice Eq. 16 can be linearized

$$\bar{b} = \frac{1}{\Delta x} \int_{-\Delta x/2}^{\Delta x/2} b(x) dx \quad [17]$$

Assuming that rotating frame relaxation and diffusion weighting are acting independently their combined effect on the signal decay during the train of GOIA-W(16,4) pulses:

$$S(t_m) = S(0) \cdot \exp[-(\bar{R}_{2\rho} \cdot t_m + (\bar{b} + b_r) \cdot \bar{D} \cdot t_m / 2T_p)]; t_m = 4m \cdot T_p; m = \overline{0, 5} \quad [18]$$

where  $t_m$  is the  $T_{2\rho}$  preparation time (multiple of four GOIA-W(16,4) pulses) and  $b_r$  is the b-value associated with the ramping of the gradient at the beginning and the end of the preparation time. The calculated b-values are 0.294, 0.589, 0.872, 1.178 and 1.473 s·mm<sup>-2</sup> for preparation times of 16, 32, 48, 64 and 80 ms, respectively (GOIA-W(16,4) of 4ms duration and 5kHz bandwidth).

We found experimentally (Fig. 6) that an effect of diffusion weighting can be observed on the signal decay in the case of  $T_{2\rho}$  preparation for 2D imaging sequences. However, the experimental effect is much higher than predicted by the above theory:

$$S(t_m) = S(0) \cdot \exp \left[ - \left( \bar{R}_{2\rho} \cdot t_m + \beta \cdot \bar{D} \cdot t_m^3 \right) \right] \quad [19]$$

with the diffusion term contributing more than linearly to the exponential signal decay. A coefficient  $\beta = 1.87 \cdot 10^6$  (mm·s)<sup>-2</sup> has found to fit both phantom and in-vivo data, resulting in b-values of 1.6, 12.8, 43.1, 102.2, and 199.6 s·mm<sup>-2</sup> for preparation times of 16, 32, 48, 64 and 80 ms are, respectively. Possible explanations for the departure between experiments and theory are considered in the Discussion section.

### 3. METHODS

#### 3.1. Simulations

Simulations for relaxation rates in the rotating frame of GOIA-W(16,4) pulses have been performed assuming the two site exchange model in the fast exchange limit (2SX/FXL) with the model parameters specified in Figure 2. A static magnetic field  $B_0$  of 2.89T (Siemens Tim Trio magnet) was assumed.

GOIA-W(16,4) pulse parameters were: 4 ms duration, 5 kHz bandwidth (time-bandwidth product  $R = 20$ ), and a gradient modulation factor  $g_m = 0.9$  (Eqs. [1,2]). Under these conditions the peak amplitude ( $B_{I,max}$ ) of the RF field was 0.382 kHz. A slice thickness of  $\Delta x = 5$  mm was considered, requiring a maximum gradient  $G_{max} = 23.49$  mT/m. A piecewise constant approach was used in all calculations by assuming that the RF field and gradient are constant over infinitesimal elements of time and space. The GOIA-W(16,4)

pulse was discretized in steps of 10  $\mu$ s, matching the experimental implementation. To account for the gradient modulation, the slice thickness has been divided in 400 thin intra-slice isochromats. Thus the number of isochromats matches the number of samples in the RF pulse waveforms. We verified that this time and slice discretization produced stable results, and further increase in digitization did not change results for two decimals precision.

The four independent parameters (correlation time constant of bound water, exchange time constant, chemical shift difference, and pool of bound water) were varied over a four dimensional grid spanning the ranges that are relevant for in-vivo conditions. The correlation and exchange time constants were varied logarithmically over four orders of magnitude ( $\tau_c \in [10^{-2}, 10^2]$  ns;  $\tau_{ex} \in [10^{-3}, 10^1]$  ms; 40 values each), while the chemical shift difference and pool of bound water were varied linearly over their range ( $P_b \in [0, 1]$ ;  $\delta\omega_{ex} \in [0, 5]$  ppm; 50 values each). In total  $4 \cdot 10^6$  combinations of model parameters were simulated. The correlation time of free water was assumed to be 5 ps, and the proton-proton distance to be 1.58 Å in both sites. Simulations were performed in Matlab 2012b (Natick, MA). Results of simulations are shown in Figures 3 and 4.

### 3.2. Pulse sequences

Pulse sequences for T1 $\rho$  and T2 $\rho$  mapping were implemented on a 3T Tim Trio clinical MR scanner (Siemens Healthcare, Erlangen). The body transmit coil, capable of 1 kHz peak RF field, was used for excitation, and a 32-channels head coil was used for signal reception. The body gradient coil of a 3T Tim Trio has a maximum gradient amplitude of 40 mT/m per axis and a rise time of 200 mT/(m·ms).

The low-power slice selective magnetization preparation module for rotating frame relaxation was realized by concatenating GOIA-W(16,4) pulses according to the MLEV4 (Levitt et al., 1982) phase cycling scheme. No gaps were introduced in the pulse train during concatenation. A single continuous pulse shape was calculated for each preparation time. The maximum preparation time was 80 ms to avoid introducing delays in the shape due to limitations with the maximum possible pulse duration. This time duration is comparable with the rotating frame relaxation time in-vivo and is sufficient to map the relevant portion of the rotating frame relaxation curve. The phase modulation of GOIA-W(16,4) was calculated dynamically for each repetition time in order to shift the slice position for multislice imaging. For T1 $\rho$ , magnetization can be intuitively visualized as making repeated flip-flops between +Z and -Z directions of the static magnetic field  $B_0$ , following the effective field of GOIA-W(16,4) pulses. For T2 $\rho$ , magnetization is first flipped perpendicular to the direction of the effective field of GOIA-W(16,4) pulses to precess around it, and at the end of preparation it is stored again along the direction of  $B_0$  field. In the case of 3D T2 $\rho$  mapping the 90° pulses bracketing the GOIA-W(16,4) pulse train were stretched adiabatic half passage hyperbolic-secant AHP-HS8 (Garwood and DelaBarre, 2001), or Shinnar-LeRoux SLR (Pauly et al., 1991) slice selective pulses for 2D T2 $\rho$  mapping. After both T1 $\rho$  and T2 $\rho$  preparation a gradient spoiler (5 ms, 25 mT/m) is used to spoil any transverse magnetization that was not stored along longitudinal direction. The prepared magnetization was sampled with a 3D turbo FLASH (TFL) or 2D spin echo EPI (EPI-SE) readout. Details of the T1 $\rho$  and T2 $\rho$  pulse sequences are given in Figure 6.

In particular, the T1 $\rho$  and T2 $\rho$  preparations for in-vivo measurements were done using: 1) GOIA-W(16,4) pulses of 4 ms and 5 kHz bandwidth, 2) preparation times of 0, 16, 32, 48, 64, 80 ms, and 3) AHP-HS8 90° pulses of 4 ms and 5 kHz bandwidth for T2 $\rho$  3D TFL, or SLR 90° pulses of 3ms and 2 kHz bandwidth for T2 $\rho$  2D EPI-SE. Shapes of the GOIA-W(16,4) pulse were sampled each 10  $\mu$ s (400 samples for 4 ms). Short ramps were needed for the GOIA-W(16,4) gradient at the beginning and the end of preparation period. The ramps were 30  $\mu$ s for the 3D TFL sequence, and 160  $\mu$ s for 5 mm slices in 2D EPI-SE. In the

case of T2 $\rho$  preparation the ramps of the GOIA gradients were refocused (balanced) with gradients of opposite sign and moment. In addition, for slice selective T2 $\rho$  the gradient of SLR 90° pulses was also balanced and superimposed on the GOIA balancing gradient. The balancing gradient was 30  $\mu$ s for the 3D TFL readout, and 480  $\mu$ s for 5 mm slices in 2D EPI-SE. The total time delay at the beginning and the end of T2 $\rho$  preparation were 60  $\mu$ s for the 3D TFL readout, and 640  $\mu$ s for the 2D EPI-SE with 5 mm slices.

The 3D TFL image acquisition was performed in sagittal orientation with the following parameters: matrix = 192 $\times$ 192 $\times$ 128, voxel size = 1.33 $\times$ 1.33 $\times$ 1.33 mm<sup>3</sup>, partial Fourier factor of 6/8 in the slice and phase encoding directions, parallel acquisition (PAT) factor 2, readout bandwidth = 1530 Hz/Pixel, flip angle = 8°, echo time TE = 0.98 ms, repetition time TR = 0.8 s, 10 dummy scans, 5 preparation times (0, 16, 32, 48, 64 ms). The total acquisition time was 5:40 min. The T1 $\rho$  and T2 $\rho$  preparation were also positioned sagittally to excite a slab of 350 mm thickness, roughly twice the right-left diameter of the head. The TR of 0.8 sec was chosen to be 8 to 10 times larger than the rotating frame relaxation times of gray and white matter tissue to allow complete relaxation of the rotating frame prepared magnetization. With this TR the SAR was 50–60% of the maximum allowed SAR (3W/kg) as monitored by the Siemens console.

The 2D EPI-SE image acquisition was performed axially with the following parameters: matrix = 128 $\times$ 128, 20 slices, voxel size = 2 $\times$ 2 $\times$ 5 mm<sup>3</sup>, partial Fourier factor of 6/8 in the phase encoding direction, interleaved slice acquisition, slice gap 50% (2.5 mm), parallel acquisition (PAT) factor 2, readout bandwidth = 1562 Hz/Pixel, excitation flip angle = 90°, refocusing flip angle = 180°, echo time TE = 27 ms, repetition time TR = 7 s (350 ms/slice), 4 dummy scans, 6 preparation times (0, 16, 32, 48, 64, 80 ms), fat suppression. The total acquisition time was 1:17 min. The slice selective T1 $\rho$  and T2 $\rho$  preparations were prescribed axially and their position was updated according to the interleaved 2D EPI-SE slice acquisition. With this TR the SAR was 80–90% of the maximum allowed SAR (3W/kg) as monitored by the Siemens console.

Importantly, for 2D imaging the slice profile of the T1 $\rho$  and T2 $\rho$  preparations have to match the slice profile of the EPI-SE sequence or any other sequence that is used for 2D image acquisition. The slice profile of GOIA-W(16,4) pulses is sharper than the slice profile of non adiabatic pulses that are typically used in the EPI-SE sequence. If slice thickness is not matched, only the central part of the EPI-SE slice will experience rotating frame relaxation while the edges will experience relaxation in the laboratory frame, resulting in a multi-exponential behavior. To avoid this situation the slice of GOIA-W(16,4) was chosen to be twice thicker (10 mm) than the slice of 2D EPI-SE (5 mm). Considering that a slice gap of 50% is typically used in 2D imaging, together with the interleaved slice excitation and sharpness of GOIA pulses, the doubling of slice thickness of GOIA pulses does not produce saturation of neighboring slices. However, the slice profiles of rotating frame preparation and image encoding can be perfectly matched if the same GOIA-W(16,4) pulses are used for refocusing in the 2D EPI-SE.

For comparison T1 $\rho$  and T2 $\rho$  mapping sequences with continuous wave spin-lock and conventional adiabatic pulses were implemented. The continuous wave (CW) spin-lock was implemented using the  $B_0$  and  $B_1$  compensation method of (Witschey et al., 2007). The conventional adiabatic preparation was implemented with stretched hyperbolic-secant HS8 pulses of 4 ms and 5 kHz bandwidth (Michaeli et al., 2008, Mangia et al., 2009). Single slice measurements were performed and compared using all three rotating frame relaxation methods CW, HS8, and GOIA-W(16,4) as detailed in the following section.

### 3.3. Phantom experiments

Two phantoms were imaged to develop and optimize our methodology. A uniform agar phantom (3% w/v) with an inner diameter of 16 cm was used to test uniformity and artifacts of rotating frame preparation. A second phantom that contained 3 agar tubes (1%, 2% and 3% w/v) immersed in saline solution was used to verify and calibrate the modeling and fitting routines.

Uniformity of multislice  $T1\rho$  and  $T2\rho$  mapping with GOIA-W(16,4) pulses was verified on the uniform phantom with both 2D EPI-SE and 3D TFL readouts. Relaxation under GOIA-W(16,4) pulses was compared with relaxation under HS8 and CW using the same image readout in single slice experiments. The  $B_{1,max}$  of HS8 was 0.886 kHz for 4 ms duration and 5 kHz bandwidth, and the  $B_{1,max}$  of CW was set to the same value as HS8. For GOIA-W(16,4) pulses two situations were considered: 1) GOIA-W(16,4) having the same duration and bandwidth as HS8 but half of the  $B_{1,max}$  (0.382 kHz), and 2) GOIA-W(16,3) pulses having similar  $B_{1,max}$  (0.821 kHz) as HS8, but half duration (2 ms) and 10 kHz bandwidth. To investigate the compensation of  $B_0$  inhomogeneity the carrier frequency during CW, HS8 and GOIA-W was placed off-resonance from the water signal, and the durations of the preparation periods were matched to the same duration (48 ms) for all measurements. Diffusion in the slice direction was measured with a pulsed gradient spin echo (PGSE) EPI sequence using five b-values in the range 200–1000  $s/mm^2$ , and matching the slice thickness and resolution of  $T2\rho$  2D EPI-SE.

### 3.4. Volunteer measurements

Brain imaging was performed on five young healthy volunteer (4 males, 1 female, 26–33 years age interval) with informed consent using a protocol approved by the IRB of our institution.  $T1\rho$  and  $T2\rho$  mapping were obtained with GOIA-W(16,4) pulses using the acquisition parameters mentioned for 3D TFL and 2D EPI-SE in Section 3.2. A structural scan was acquired at 1 mm isotropic resolution with the MEMPRAGE sequence (van der Kouwe et al., 2008) to perform brain segmentation and statistical analysis of  $T1\rho$ ,  $T2\rho$  and molecular parameters in region of interests (ROI) of the brain. Diffusion in the slice direction was measured with a pulsed gradient spin echo (PGSE) EPI sequence using five b-values in the range 200–1000  $s/mm^2$ , and matching the slice thickness and resolution of  $T2\rho$  2D EPI-SE.

### 3.5. Data analysis

Maps of relaxation time constants were calculated by fitting a mono-exponential law  $S_{1\rho,2\rho}(t) = S(0)\exp(-t/T_{1\rho,2\rho})$  to the phenomenological relaxation curves measured for  $T1\rho$  with 3D or 2D sequences and  $T2\rho$  with 3D sequences. In practice a first order polynomial was fit to the log-linear time series signal to obtain the relaxation rates. In the case of  $T2\rho$  relaxation measured with 2D sequences Eq. [19] was fit to the data using the diffusion constant that was independently estimated from PGSE measurements.

To extract parametric maps of correlation times, exchange times, water bound fraction, and chemical exchange frequency the experimental time series were fitted according to the 2SX/FXL model from Eqs. 5–8 and assuming the GOIA-W(16,4) modulation functions of Eqs. 1–3. The slice or slab thickness was considered for both 2D and 3D measurements. For 2D measurements 500 isochromats were considered for each slice as mentioned for simulations. For 3D measurements since the slab excited by  $T1\rho$  and  $T2\rho$  preparations was much thicker (350 mm) than the individual slice thickness (1.33 mm), each slice was considered its own isochromat. This was verified to give stable results compared to the case when more isochromats were calculated for each slice. The slice position within the 3D slab was included in the calculation. However, since the maximum gradient for a 350 mm slab is very

weak ( $G_{max} = 0.34$  mT/m in Eq. [2]) no effect of slice position within the brain was detected on the measured  $T1\rho$  and  $T2\rho$  relaxation times. As mentioned earlier, for 2D acquisition the effect of slice position is completely removed by the frequency modulation that is needed to shift the slice position. Nonlinear curve fitting of time series signal was employed to obtain the model parameters.

All fitting was performed in Matlab R2012b (Natick, MA). Each voxel was fit independently and parallel computation toolbox was used to speed up calculations. The fitting was done in the least square sense for both linear and nonlinear curve fitting.

An ROI analysis was done for all the maps. The structural 3D MEMPRAGE image was segmented using Freesurfer 5.1 software (Fischl et al., 2002) and then coregistered using the bregister (Greve and Fischl, 2009) method of Freesurfer to the maps derived from 3D  $T1\rho$  and  $T2\rho$  measurements. Mean values and standard deviations were calculated for eight brain ROIs (cortical gray matter, white matter, thalamus, caudate, putamen, pallidum, hippocampus, ventral diencephalon that includes substantia nigra). Only the voxels with an  $R^2$  coefficient of determination larger than 0.95 were included in the statistical analysis. Edge voxels at the border of two ROIs were excluded to reduce ambiguity in classification and coregistration. Hundreds to a few thousands voxels were available in each ROI for statistical analysis.

## 4. RESULTS

### 4.1. Simulations of rotating frame relaxation and diffusion weighting under GOIA pulses

In Figure 1(G,H) simulations of the slice profiles at the isocenter and off-isocenter locations are shown for an inversion GOIA-W(16,4) pulse of 4 ms duration, 5 kHz bandwidth, 0.382 kHz maximum RF amplitude and slice thickness of 5mm (Eqs. [1–3]). Note, in all subsequent simulations the same GOIA-W(16,4) and slice thickness have been assumed. The slice profile at the isocenter is characterized by 100% inversion in the center of the slice and 98% inversion at the edge of the flat top, transition bands (flat top to baseline) that represent 40% of the slice thickness, one very small sideband with less than 3% inversion symmetrically on each side of the slice. The slice at the off-isocenter position shows a very similar profile with minimal smearing due to the gradient versing. Increasing the BW of the pulse reduces the transition bands and can eliminate completely the sidebands at the cost of increased  $B_{1,max}$ . However, the pulse of Fig. 1 represents a good compromise between inversion performance, slice selectivity, duration and  $B_{1,max}$  requirements.

Simulations of rotating frame relaxation rates for the same GOIA-W(16,4) pulse and assuming a 2.89T static magnetic field. In Figure 3 longitudinal (Fig. 3A,B) and transverse (Fig. 3C,D) rotating frame relaxation rates for dipolar coupling and exchange interactions were calculated (Eqs. [5,6]) over the range of correlation and exchange time constants expected in-vivo. The bound water fraction  $P_b$  was assumed 0.2 and the exchange chemical shift difference  $\delta\omega_{ex}$  was considered 0.8 ppm ( $\sim 100$  Hz at 2.89T). Due to pulse modulation the relaxation rates are time dependent, reaching a maximum ( $R_{1\rho}$ ) or a minimum ( $R_{2\rho}$ ) in the middle of the pulse. The exchange  $T1\rho$  relaxation time constant (Fig. 3B) exhibits a maximum around an exchange time constant of 3 ms. The other relaxation rates increase with the correlation (Fig. 3A,C) and exchange time constants (Fig. 3D). This is a similar behavior as noticed for conventional adiabatic pulses in the absence of magnetic field gradients (Michaeli et al., 2008, Mangia et al., 2009).

In Figure 4 the observed longitudinal (Fig. 4A,B) and transverse (Fig. 4C,D) rotating frame relaxation rates are simulated assuming the 2SX/FXL model for several combinations of model parameters. The four dimensional parameter space was sampled over ranges relevant

for in-vivo conditions and FXL regime ( $\tau_{c,f}$  was fixed at 5 ps). The correlation time and exchange time constants were sampled logarithmically over four orders of magnitude, while the exchange range and water bound fraction were sampled linearly. For each slice isochromat the time average relaxation was first calculated according to Eqs. [7,8] and then the slice averaged relaxation was obtained using Eq. [9]. Model parameters were assumed not to vary across isochromats (this is discussed in the case of Fig. 5). Figs. 4A,C show the hyperplanes through the four dimensional space when two of the model parameters are fixed: bound water fraction  $P_b$  of 0.15 and exchange rate  $\delta\omega_{ex}$  of 0.8 ppm. The longitudinal rotating frame relaxation rate (Fig. 4A) exhibits a steep increase with correlation time constant in the 0–5 ns interval, and a smaller increase in the 5–10 ns interval. The change over the exchange time constant is less pronounced compared to change over the correlation time constant, indicating that dipolar coupling is the major relaxation mechanism. The transverse rotating frame relaxation rate (Fig. 4C) shows slightly larger changes across correlation and exchange time constants. However, the interplay between dipolar coupling and exchange interactions can change based on the water pools populations and exchange rates. In Figs. 4B,D a hyperplane through the four dimensional space is shown when the correlation time constant  $\tau_{c,b}$  was fixed at 2 ns and the exchange time constant  $\tau_{ex}$  was set to 0.2 ms. These values are relevant for in-vivo conditions and fulfill the fast exchange condition. The longitudinal (Fig. 4B) and transverse (Fig. 4D) rotating frame relaxation rates exhibit almost a linear dependency on water bound fraction in the FXL regime. A parabolic dependency starts to become evident, as expected from Eqs. [6] when bound water fraction or exchange rate increase.

Figures 4E,F show the isosurfaces through the parameter space corresponding to particular values of rotating relaxation times  $T1\rho = 90$  ms and  $T2\rho = 85$  ms. While the parameter space and number of solutions that can fit each relaxation is very large, the intersection of both spaces is relatively small and indicate that combining longitudinal and transverse rotating relaxation can lift this degeneracy and converge the fit on a small number of solutions for model parameters.

In Figure 5 the isochromat dependency on relaxation and diffusion are illustrated. Figure 5A shows the progressive inversion of the magnetization as the pulse sweeps through each isochromat of the slice. It can be seen that the assumption of instant magnetization inversion of each isochromat a good approximation. Although the inversion at the end of the pulse is perfectly confined to the slice it can be noticed that at intermediate times, particularly in the middle part of the pulse between 1–3 ms, magnetization outside of the slice is slightly affected. Magnetization may be temporarily flipped up to 40% in the immediate vicinity of the slice in regions extending out up to half of slice thickness from the edge of the slice. This effect becomes small beyond this limit and is unnoticeable at a distance of 15 mm (3 times the slice thickness). With interleaved slice acquisition and 50% slice gap the rotating frame magnetization history between chronologically excited slices can be avoided. The inversion times for each isochromat are plotted in Fig. 5B, which as expected show faster inversion at the edges of the slice where the pulse is swept faster.

Simulations performed in Fig. 5C–F show that there is very little difference in the average relaxation rates obtained by the exact calculation of Eqs. [7–9] or approximate calculation of Eqs. 10. A single value was assumed for each model parameter ( $\tau_{c,b} = 2$  ns,  $\tau_{ex} = 0.2$  ms,  $\delta_{ex} = 0.8$  ppm,  $P_b = 0.15$ ,  $\tau_{c,f} = 5$  ps) and equal distribution of initial magnetization across isochromats. Using the exact calculations Eqs. [7–9], a symmetric distribution is obtained, with less than 3% difference between the relaxation rates of different isochromats. This explains why the linearization and calculation with Eqs. [10] yields very close results. Although these results are contingent on the assumption that model parameters are the same for all isochromats, even when including a variation of  $\pm 25\%$  for the model parameters

across the slice thickness the average values calculated by Eqs. [7–9] or Eqs. [10] differ by less than a 5%. For thin slices ( $\leq 5$  mm) a limited variation of model parameters across slice thickness may be an acceptable assumption.

Figures 5G,H plot the gradient moment and b-values as a function of isochromat calculated using Eqs. [12–15] for a pair of GOIA-W(16,4) pulses. A symmetric distribution of b-values is obtained. The b-values are much higher at the edge of the slice compared to the middle part, which is expected since the gradient is much stronger for the isochromats at the edge of the slice. The difference between the mean b-value of the slice calculated with the exact Eq. [16] or approximate Eq. [17] approach is very small because the first order contribution dominates in the Taylor expansion of the exponentials. A diffusion coefficient of  $0.8 \cdot 10^{-3} \text{ mm}^2 \cdot \text{s}^{-1}$  was considered for all isochromats.

#### 4.2. Experimental diffusion weighting during GOIA pulse trains

First, the possible effects of diffusion on the signal decay during the gradient modulated GOIA-W(16,4) pulse train were investigated experimentally for both  $T1\rho$  and  $T2\rho$  relaxations. Measurements performed in an agar phantom and volunteers are presented in Figure 7. Relaxation curves were measured using GOIA-W(16,4) pulses of 4 ms for two situations: 1) a strong gradient ( $G_{max} = 23.5 \text{ mT/m}$ ) used to prepare  $T1\rho$  and  $T2\rho$  for a 5 mm slice, and 2) a very weak gradient ( $G_{max} = 0.34 \text{ mT/m}$ ) used to prepare  $T1\rho$  and  $T2\rho$  for a 350 mm thick slab. In both cases a single slice of 2.5 mm was acquired with the 2D EPI-SE sequence in the middle of the region prepared by rotating frame relaxation. The experiment with the weak gradient did not produce any detectable diffusion weighting, and in this respect is similar with the spatially non-selective rotating frame relaxation.

In the case of  $T1\rho$  experiments (Figs. 7A,C) the experimental relaxation curves obtained for the 5 mm slice (red diamonds) and the 350 mm thick slab (black circles) are identical and can be fitted with a mono-exponential function in both agar phantom (Fig. 5A,  $T1\rho = 71 \text{ ms}$ ) and volunteers (Fig. 5C,  $T1\rho = 87 \text{ ms}$ ), proving that diffusion weighting does not affect  $T1\rho$  measurements. In the case of  $T2\rho$  experiments (Figs. 5B,D) the effects of diffusion become apparent as the signal decay curves for the 5 mm slice and the 350 mm thick slab are different. As expected for diffusion weighting, the difference between  $T2\rho$  signal decay curves measured in the thin slice (red diamonds) and thick slab (black circles) increases with diffusion coefficient (agar  $D = 2.1 \cdot 10^{-3} \text{ mm}^2 \cdot \text{s}^{-1}$ , white matter  $D = 0.8 \cdot 10^{-3} \text{ mm}^2 \cdot \text{s}^{-1}$ ). The signal decay for the 5 mm slice selective  $T2\rho$  measurements can be fitted empirically by Eq. [19], which includes in the exponential a non-linear time contribution of the diffusion term in addition to transverse rotating relaxation. Good agreement between Eq. [19] (red dashed line) and the 5 mm slice experimental time points (red diamonds) is obtained using the same transverse rotating frame relaxation rate that fits the 350 mm thick slab relaxation (black circles and line) and the diffusion constant measured from the PGSE (agar  $T2\rho = 52 \text{ ms}$  and  $D = 2.1 \cdot 10^{-3} \text{ mm}^2 \cdot \text{s}^{-1}$  in Fig. 5B, in-vivo  $T2\rho = 68 \text{ ms}$  and  $D = 0.8 \cdot 10^{-3} \text{ mm}^2 \cdot \text{s}^{-1}$  in Fig. 5D). The same  $\beta$  coefficient ( $1.87 \cdot 10^6 \text{ mm}^{-2} \cdot \text{s}^{-2}$ ) fits both phantom and volunteer data, and is characteristic for the particular GOIA pulse used. The corresponding b-values are, respectively, 1.6, 12.8, 43.1, 102.2, and  $199.6 \text{ s} \cdot \text{mm}^{-2}$  for  $T2\rho$  preparation times of 16, 32, 48, 64 and 80 ms. These experimental b-values are much larger as predicted from Eqs. [12–16]. This is further analyzed in the Discussion section.

#### 4.3. Measurements of GOIA rotating frame relaxation in phantoms

Results obtained on the agar phantoms are presented in Figures 8–10. Figure 8A shows the  $T1\rho$  and  $T2\rho$  relaxation maps obtained on the uniform agar phantom with GOIA-W(16,4) pulses, HS8 pulses and CW spin-lock. GOIA-W(16,4) pulses that match either the duration of the HS8 pulses (abbrev. GOIA4 for 4 ms duration) or the amplitude of HS8 pulses

(abbrev. GOIA2 for 2 ms duration) have been used. The amplitude of CW spin-lock matched the amplitude of HS8 pulses. As shown previously (Michaeli et al., 2008, Mangia et al., 2009) relaxation times depend on the modulation functions, and longer relaxation times are measured with adiabatic pulses of higher  $B_{1,max}$ . The shortest T1 $\rho$  and T2 $\rho$  relaxation time constants are measured with CW spin-lock, which also shows the smallest difference between longitudinal and transverse relaxation times. This is expected since CW spin-lock acts on magnetization that is in the transverse plane for both T1 $\rho$  and T2 $\rho$  relaxation, while adiabatic pulses act on longitudinal magnetization in the case of T1 $\rho$  relaxation and transverse magnetization for T2 $\rho$  relaxation. The uniformity of multislice T1 $\rho$  and T2 $\rho$  imaging with GOIA-W(16,4) pulses is proven in Fig 8B. The sagittal views taken along the slice direction indicate no saturation or magnetization history between slices. In Fig. 8C the effect of  $B_0$  inhomogeneity was investigated. The carrier frequency of pulses was shifted off-resonance from the water as noted on the left side. Despite using the  $B_0$  and  $B_1$  compensation scheme for CW spin-lock (Witschey et al., 2007) the compensation of the offset is not perfect and works for a limited range of offsets. Artifacts are observed for offsets over 100 Hz. Adiabatic pulses exhibit a much better compensation and image uniformity across a wide range of offsets.

Molecular dynamics parameters in the agar phantom were estimated by fitting the 2SX/FXL model to the relaxation measurements from Fig 8A. In order to restrict the possible solution space of the non-linear least square fit the data from both T1 $\rho$  and T2 $\rho$  measurements were used. As shown by simulations (Figs. 4E,F) the intersection of the two solution spaces is very small. The maps of correlation time constant, exchange time constant, water bound fraction and chemical exchange difference that best fit the experimental data are shown in Figure 9. The range of values for the molecular parameters is much smaller compared to the values of relaxation times obtained with different approaches. While the relaxation time constants depend on both sample and the pulse sequence, molecular parameters are sample specific and are more appropriate for quantitation and comparing measurements done with different techniques if the same relaxation model is used for fitting.

Figure 10 shows results obtained on the multi-compartment agar phantom with GOIA-W(16,4) pulses of 4 ms and 5 kHz. Relaxation and parameter maps of molecular dynamics are shown in the upper two rows. It can be seen that T1 $\rho$  and T2 $\rho$  relaxation maps show visible contrast between tubes differing only by 1% in agar concentration. T1 $\rho$  relaxation times were:  $135.8 \pm 5.1$  ms for 1% agar,  $107.4 \pm 4.8$  ms for 2% agar, and  $84.2 \pm 3.5$  ms for 3% agar. T2 $\rho$  relaxation times were:  $119.3 \pm 4.6$  ms for 1% agar,  $97.2 \pm 4.1$  ms for 2% agar, and  $72.3 \pm 3.9$  ms for 3% agar. Differences are noted also in the maps of the molecular dynamics parameters. Importantly, the bound water fraction ( $P_b$ ) map is sensitive to the difference in agar concentration. The bound water fraction was found to be  $4.8 \pm 0.3\%$  for 3% agar,  $3.1 \pm 0.3\%$  for 2% agar and  $1.9 \pm 0.2\%$  for 1% agar. The bound water fractions derived from the relaxation measurements are slightly higher than the agar weight/volume ratio that was used to prepare the phantoms. This may be explained by the syneresis phenomenon of agar hydrogels which are known to expel water (Boral et al., 2010). A layer of water was macroscopically observed at the interface between the agar gel and the wall of the tubes. The maps in the bottom row of Fig. 10 show the  $R^2$  coefficient of determination of the fitting. For T1 $\rho$  and the 2SX/FXL model fitting the  $R^2$  values are above 0.99 inside agar tubes. For T2 $\rho$  fit the  $R^2$  values are above 0.9 inside agar tubes.

In order to investigate whether model parameters would be overfitted when using relaxation data measured with a single GOIA modulation we also fitted model parameters from dispersion data obtained at multiple GOIA modulations in the uniform agar phantom. For this purpose, T1 $\rho$  relaxation decay curves were acquired at four different GOIA modulations and the T1 $\rho$  relaxation constants were derived first. The four T1 $\rho$  relaxation constants were

further used as input data for the model fitting. Independently, the model parameters were estimated also by fitting the relaxation decay curve measured with a fifth GOIA modulation that was different from the four dispersion GOIA modulations. It was found that the main difference lies in the fitted  $\tau_{c,b}$  correlation time constants which differ by approximately 11%. The fits of the exchange time constant  $\tau_{ex}$ , exchange chemical shift  $\delta\omega_{ex}$ , and water bound fraction  $P_b$  are very similar, and differ by less than 4%. It can be also noticed that the standard deviations of the dispersion fits are smaller. However, the differences noticed between the two fits are much smaller compared to the range of variation obtained for example when agar concentration was varied by 1% as in Fig. 10. The results are summarized in Table 1.

#### 4.4. Measurements of rotating frame relaxation in volunteers

Results obtained from the  $T1\rho$  and  $T2\rho$  measurements performed on volunteers are summarized in Figures 11–15. Relaxation in the rotating frame has been prepared with GOIA-W(16,4) pulses of 4 ms duration, 5 kHz bandwidth, and 0.382 kHz peak RF amplitude.

Figure 11 shows 3D maps of  $T1\rho$  and  $T2\rho$  relaxation times acquired in the brain at 1.33 mm isotropic resolution in 5:40 min using the 3D TFL image readout. Three orthogonal sections are shown for both maps. The  $T1\rho$  map shows good uniformity across brain in all three sections. The  $T2\rho$  map shows some signal loss in regions of the pons and cerebellar vermis, which are near the base of the skull close to big air cavities such as pharynx. This signal loss is related to areas of large  $B_0$  inhomogeneity which leads to additional dephasing of transverse magnetization that precess around the effective field during the  $T2\rho$  preparation. In the case of  $T1\rho$  mapping the longitudinal magnetization is locked along the effective adiabatic field and its evolution is not susceptible to  $B_0$  inhomogeneities.

Figure 12 shows 2D multi-slice maps of  $T1\rho$  and  $T2\rho$  relaxation times from the brain of the same volunteer acquired in 1:17 min with slice selective rotating frame preparation and 2D EPI-SE readout. Four axial slices were selected for display at different levels in the brain, i.e. centrum semiovale, ventricles, and infratentorial. The coronal view on the right side shows the prescription of all slices and proves, as in the phantom case, that multislice excitation can be obtained without saturation and magnetization history. The effects of  $B_0$  inhomogeneity are observed in  $T2\rho$  maps towards the base of the skull. Diffusion coefficients were independently measured to separate the diffusion weighting from the  $T2\rho$  relaxation in the signal decay curves.

Maps of molecular dynamics parameters were calculated using the 2SX/FXL model to fit the 3D rotating frame relaxation measurements, and results are presented in Figure 13. Again as in the phantom case, the data from both  $T1\rho$  and  $T2\rho$  measurements were used in order to restrict the possible solution space of the non-linear least square fit. Since in the case of 3D mapping the slab inverted by the GOIA-W(16,4) was very thick (350 mm) while on the other hand each slice in the 3D volume was much thinner (1.3 mm) we can safely use Eqs. [10] and assume there is little variation of model parameters across each thin slice. All parameter maps show good uniformity and contrast across the brain in all three orthogonal directions that are displayed. Anatomical features of the cortical and subcortical structures can be easily noticed. Segmentation of the  $T1\rho$ ,  $T2\rho$  and parametric maps of molecular dynamics are shown in Figure 14. At 1.33 mm isotropic resolution the boundaries between cortical gray matter, white matter, and subcortical structures can be followed on all the maps. Mean values and standard deviations of rotating frame relaxation time constants, correlation time constants, exchange time constants, and bound water fraction in eight ROIs of the brain are plotted in Figure 15. The values for all parameters are also given in Table 2. A difference (contrast) of 20–30% among mean parameter values of different brain

structures is noticed. Only the voxels with an  $R^2$  coefficient of determination larger than 0.95 were included in the statistical analysis. Except for CSF, the majority of voxels (~99% for  $T1\rho$ , and ~85% for  $T2\rho$ ) in the brain parenchima had  $R^2 > 0.95$ . Values of the molecular dynamics parameters were in the range of values reported in the literature for in-vivo measurements (Michaeli et al., 2008, Sierra et al., 2008, Jokivarsi et al., 2009, Mangia et al., 2009).

## 5. DISCUSSIONS

The use of GOIA-W(16,4) pulses solves simultaneously three major problems in  $T1\rho$  and  $T2\rho$  mapping: i) reduction of SAR, ii) compensation of  $B_1$  and  $B_0$  inhomogeneity, and iii) slice selectivity. The last aspect is relevant particularly for 2D imaging, while the second aspect is specifically improved when compared to CW approaches. Consequently, GOIA-W(16,4) pulses allow for faster and more robust imaging of  $T1\rho$  and  $T2\rho$  relaxation in both 2D and 3D sequences.

Compared to the more familiar T1 and T2 relaxation in the laboratory frame, the  $T1\rho$  and  $T2\rho$  relaxation in the rotating frame are weighted more towards water molecules interacting with macromolecules. The water bound fraction experience dynamics on the ns-ms time scale which is better accessed with the weaker  $B_1$  radiofrequency field (~10 $\mu$ T) than with the stronger  $B_0$  static field (~1T). In addition, the  $B_1$  field can be easily varied compared to the  $B_0$  field, enabling detailed investigation of relaxation mechanisms via relaxation dispersion curves. Modulation functions of adiabatic pulses can be varied too, adding more versatility than CW spin-lock. In the case of GOIA pulses simultaneous modulation of the RF field and gradient enables shorter pulses in-vivo within the limits of available  $B_{1,max}$  and SAR, which provides more flexibility for preparation times. Another effect leading to further decrease of SAR is related to the fact that relaxation times scale with the size of the effective field. Relaxation time constants are longer under the higher effective field of conventional adiabatic HS4 pulses, and shorter under the smaller effective field of GOIA-W(16,4). A comparison of the frequency sweep and time evolution of the nutation angle between the two pulses indicate that frequency is swept slower in the middle of the pulse and magnetization spends more time in the region near to the transverse plane in the case of GOIA-W(16,4) pulse, which may explain shorter rotating relaxation time constants. To accurately measure relaxation times the duration of magnetization preparation has to approach the relaxation time constant. Hence, the longest preparation time with HS4 pulse may need to exceed 100 ms (Mangia et al., 2009), while for GOIA-W(16,4) pulses 80 ms preparation may be sufficient. Reduced SAR with GOIA-W(16,4) pulses might facilitate the use of  $T1\rho$  and  $T2\rho$  relaxation at higher fields (7T) in humans.

Often rotating frame relaxation experiments performed under CW spin-lock try to match the amplitude of the RF field to a certain value for the molecular dynamics parameter of interest. In-vivo this might not be necessary or counterproductive since tissue conditions are spatially heterogeneous. For example, pH variations in disease could change exchange rates across the lesion. Adiabatic pulses with their sweep of frequency might actually be suited to address this spatial heterogeneity of molecular parameters. GOIA-W(16,4) pulses have a slow linear frequency sweep over the central part of the pulse (aprox. 45% of the pulse duration). The sweep of GOIA-W(16,4) over the middle part of the pulse is slower compared to HS4 pulses, which might be more advantageous to step through the range of values for in-vivo molecular dynamics parameters.

The use of a slice selective gradient during  $T1\rho$  and  $T2\rho$  could result in relaxation rates being sensitive to slice position or diffusion. These two aspects are relevant only for 2D imaging, since in 3D sequences the gradient is very weak (0.34 mT/m). First, as proven in

the theory and experiments, the dependency on the slice position is removed from the relaxation curve by the frequency modulation used to excite slices off-isocenter. The dependency of the relaxation rate on intra-slice isochromats can be calculated and a slice mean relaxation rate can be exactly computed. Second, diffusion may play a role only during 2D  $T2\rho$  preparation. Signal attenuation can be fitted with a combined  $T2\rho$  relaxation and diffusion equation. In the case of  $T1\rho$  preparation longitudinal magnetization is locked along the adiabatic effective field and signal attenuation due to diffusion cannot occur. The b-values for a particular GOIA-W(16,4) pulse can be calibrated on phantoms. We found that experimental b-values are smaller than  $200 \text{ s}\cdot\text{mm}^{-2}$  for  $T2\rho$  preparation times up to 80 ms. However, the experimental b-values are much larger than those predicted by the theory employed in the theory section. Several possible explanations for the departure between theory and experiment may exist. First the theoretical derivation of b-values is based on the assumption of instantaneous inversion of isochromats, a reversal of the gradient moment and the exact cancellation of the radiofrequency contribution to the phase scrambling. However, slight imperfections in the gradient and RF waveforms, such as delays between the two waveforms or phase inaccuracies in the RF modulation may render this assumption less accurate. In this case the phase scrambling due to the radiofrequency term may not cancel but accumulate over the preparation time. Second, the contribution to the diffusion of the magnetization from the transition bands was not included. The b-values in the transition bands are larger than in the center of the slice, however the magnetization trajectory is more complicated. Third, an imperfect inversion of the magnetization in the presence of the gradient could accumulate over the pulses, however such an effect would be more linear and should be visible in both  $T1\rho$  and  $T2\rho$  experiments. Fourth, crossterms from other imaging gradients were not included, although the effect of the ramps was considered. Fifth, a possible crossterm between rotating frame relaxation and diffusion may exist if the time scale of molecular dynamics and diffusion were similar. While the dipolar coupling is much faster than diffusion, the exchange interaction could happen on a similar time scale like diffusion. However considering also the length scale and the strength of the macroscopic gradient this is a less likely situation.

On the other hand, a magnetization preparation module that simultaneously probes relaxation in the rotating frame and diffusion could be useful. When analyzed separately, ADC and rotating frame relaxation rates correlate strongest with disease stage and treatment response (Kettunen et al., 2007, Jokivarsi et al., 2010b). It may be plausible that a combined diffusion-relaxation contrast might show even more specificity and sensitivity to pathology, linking macromolecular fraction and cell density. By analogy, relaxation along the fictitious field that combines  $T1\rho$  and  $T2\rho$  relaxation seems to correlate stronger with pathology than either relaxation alone (Liimatainen et al., 2012). Diffusion weighting during GOIA-W(16,4) pulse can be adjusted by the gradient modulation factor. Moreover, the gradient modulation during  $T2\rho$  preparation is periodic, resembling the oscillating gradient diffusion (OSGE) method (Aggarwal et al., 2012), and the frequency of oscillation can be changed by changing pulse duration. These features provide flexibility in tuning the diffusion component of the sequence.

For slice selective  $T1\rho$  and  $T2\rho$  relaxation it is important that the slice profiles of magnetization preparation and the imaging readout are matched. This can be perfectly achieved in spin echo sequences that use the same GOIA-W(16,4) pulses for preparation and readout. The slice profile of GOIA-W(16,4) pulses is sharper than for typical pulses used in MRI sequences. Doubling the slice thickness of the GOIA-W(16,4) pulses ensures that all the magnetization that is imaged is also prepared by the rotating frame relaxation, if different pulses are used for readout. With a slice gap of 50% the neighboring slices are not excited and magnetization saturation does not occur. Also interleaved slice acquisition provides a temporal separation of  $2\cdot\text{TR}$  between adjacent slices allowing more time for

relaxation and magnetization recovery to proceed compared to a single TR in spatially non-selective rotating frame relaxation. While slice selectivity could also be obtained with conventional adiabatic pulses using a gradient, GOIA pulses offer the advantage of 80% less SAR for the same duration and bandwidth. Obviously slice selectivity cannot be achieved for CW by applying a gradient during spin-lock, and GOIA-W(16,4) pulse has 20% less SAR compared to a CW spin-lock of the same peak amplitude.

Maps of  $T1\rho$  relaxation time obtained with GOIA-W(16,4) pulses show good uniformity and no artifacts over the entire brain in human volunteers. The  $T2\rho$  relaxation maps show artifacts as signal loss in structures at the base of the skull (pons, cerebellar vermis), that are located in the vicinity of big air cavities. This is due to large  $B_0$  inhomogeneity in these regions, resulting in dephasing the precession of transverse magnetization around the effective field.

Previous investigators showed that parameters of molecular dynamics can be calculated from rotating frame relaxation curves (Michaeli et al., 2006, Michaeli et al., 2008, Sierra et al., 2008, Jokivarsi et al., 2009). We show here, for the first time to our knowledge, 3D maps of water molecular dynamics in the human brain. Molecular dynamics parameters depend solely on tissue properties, and represent a more useful quantification that is suited for comparing results among different investigators. Relaxation rates depend on both the tissue properties and sequence, which leads to variability among results reported by different investigators. For a given relaxation model, such as 2SX/FXL, the fitted molecular parameters are independent of the measurement method and reflect more faithfully the intrinsic properties of the tissue. Of particular interest is the map of the bound water fraction, which correlates with the macromolecular content. A change of 1% in the macromolecular content could be detected in agar phantoms. In the brains of young healthy volunteers 20–30% contrast has been observed in the maps of bound water fraction among different brain structures. This suggests the possibility that such an approach may be able to discover subtle differences across the entire brain in neurological diseases.

Caution has to be exercised regarding overfitting the relaxation curves. Our relaxation curves had five or six time points, while our model had four free parameters, hence the system is overdetermined. However, due to the system of non-linear equations multiple solutions are possible. By restricting the possible range of each parameter and selecting the starting point appropriately for in-vivo conditions, the solution space can be narrowed. One more free parameter can be eliminated by fixing the chemical shift exchange difference. In our case a value of 0.45 ppm (~50 Hz at 2.89T) fits well the in-vivo data. Additionally, to reduce more the ambiguity in determining the model parameters dispersion data can be collected at different modulations of the RF field or by combining  $T1\rho$  and  $T2\rho$  relaxation. Our results from the agar phantom indicate that the difference in the parameter fits is relatively small when using dispersion versus single relaxation data, and compares favorably with the differences noticed at different agar concentrations or between gray and white matter. This is particularly true for the water bound fraction, which may be the most meaningful and useful parameter. On the other hand, acquiring dispersion data would be difficult to do routinely in patients due to increased acquisition time and the higher likelihood of motion artifacts. Further research and development is necessary to find the best and most feasible strategy to derive accurate model parameters.

Although the relaxation model that we adopted excludes other possible relaxation mechanisms such as auto-relaxations, cross-relaxations and cross-correlations, it is a good compromise in explaining the experimental data while maintaining the complexity within practical limits. More advanced in-vivo relaxation models using three spins system and additional relaxation channels have been discussed (Michaeli et al., 2008) but the number

degrees of freedom quickly increases, leading to assumptions for the value of certain parameters.

Alternative methods to rotating frame relaxation have been proposed for investigating the macromolecular content, such as magnetization transfer - MT (Hu et al., 1992), and chemical exchange saturation transfer - CEST (Zhou et al., 2003). All these methods share in common the concept of creating contrast by preparing magnetization with spatially non-selective RF irradiation. Spatial selectivity can be easier incorporated with relaxation in the rotating frame than with MT and CEST.

The current work has implications also for other applications of  $T_{1\rho}$  relaxation, such as functional activation studies (Hulvershorn et al., 2005), cerebral metabolic rate of oxygen consumption (CMRO<sub>2</sub>) (Mellon et al., 2010), and pH imaging (Kettunen et al., 2002, Kogan et al., 2012). Multi-slice and faster acquisition with GOIA-W(16,4) pulses should benefit these applications too. Our method can be used also outside the brain.

For clinical applications it is expected that the proposed sequences are more robust and patient friendly in a clinical environment, providing high-resolution whole head measurements in feasible scan time. In particular, the selective multislice acquisition in roughly 1 min could be useful to translate rotating frame relaxation mapping in humans with acute stroke, where  $T_{1\rho}$  has been shown to predict time to onset in animal models (Jokivarsi et al., 2010a).

## 6. CONCLUSIONS

In summary, we demonstrated a new imaging method for relaxation in the rotating frame that addresses several limitations of the existing methods. The improvements shown for SAR reduction, compensation of  $B_0$  and  $B_1$  inhomogeneity related artifacts, and spatial selectivity may facilitate the routine acquisition of  $T_{1\rho}$  and  $T_{2\rho}$  relaxation maps in clinical examinations. Validation studies in patients are necessary, and further development of the proposed method at 3T and 7T may provide new contrast.

## Acknowledgments

Funding provided to O.C.A. by the KL2 MeRIT award from the Harvard Clinical and Translational Science Center (8KL2TR000168-05) and the K22 Career Development Award from the National Cancer Institute of the National Institutes of Health (K22 CA178269-01). Resources provided to Martinos Center by the Center for Functional Neuroimaging Technologies, P41EB015896, a P41 Regional Resource supported by the National Institute of Biomedical Imaging and Bioengineering (NIBIB), National Institutes of Health. This work also involved the use of instrumentation supported by the NIH Shared Instrumentation Grant Program and/or High-End Instrumentation Grant Program, specifically grant S10RR021110. Discussions with Dr. Michael Garwood, Dr. Shalom Michaeli, Dr. Silvia Mangia and Dr. Wolfgang Bogner are gratefully acknowledged.

## References

- Abragam, A. Principles of Nuclear Magnetism. New York: Oxford University Press; 1961.
- Aggarwal M, Jones MV, Calabresi PA, Mori S, Zhang JY. Probing mouse brain microstructure using oscillating gradient diffusion MRI. *Magnetic Resonance in Medicine*. 2012; 67:98–109. [PubMed: 21590726]
- Andronesi OC, Ramadan S, Ratai EM, Jennings D, Mountford CE, Sorensen AG. Spectroscopic imaging with improved gradient modulated constant adiabaticity pulses on high-field clinical scanners. *Journal of Magnetic Resonance*. 2010; 203:283–293. [PubMed: 20163975]
- Aronen HJ, Ramadan UA, Peltonen TK, Markkola AT, Tanttu JI, Jaaskelainen J, Hakkinen AM, Sepponen R. 3D spin-lock imaging of human gliomas. *Magnetic Resonance Imaging*. 1999; 17:1001–1010. [PubMed: 10463651]

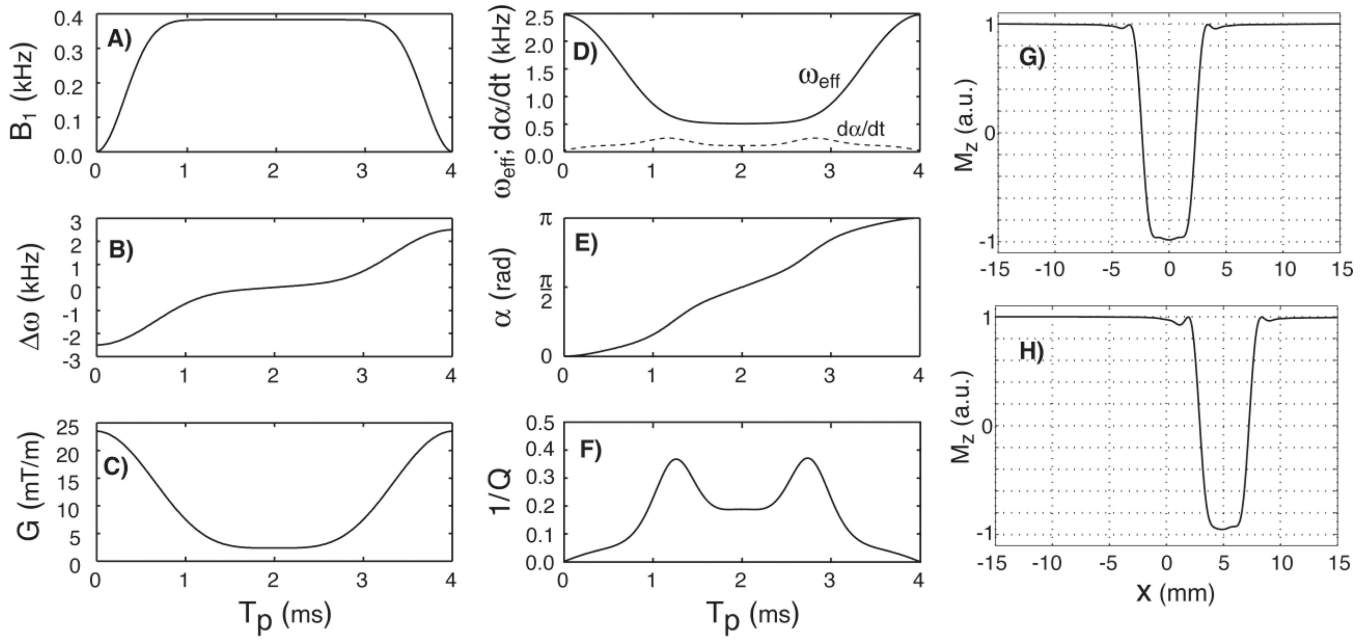
- Blicharski J. Nuclear magnetic relaxation in rotating frame. *Acta Physica Polonica*. 1972; 41:223–236.
- Boral S, Saxena A, Bohidar HB. Syneresis in agar hydrogels. *Int J Biol Macromol*. 2010; 46:232–236. [PubMed: 20035783]
- Borthakur A, Sochor M, Davatzikos C, Trojanowski JQ, Clark CM. T1(rho) MRI of Alzheimer's disease. *Neuroimage*. 2008; 41:1199–1205. [PubMed: 18479942]
- Conolly S, Nishimura D, Macovski A, Glover G. Variable-Rate Selective Excitation. *Journal of Magnetic Resonance*. 1988; 78:440–458.
- Duvvuri U, Poptani H, Feldman M, Nadal-Desbarats L, Gee MS, Lee WM, Reddy R, Leigh JS, Glickson JD. Quantitative T1rho magnetic resonance imaging of RIF-1 tumors in vivo: detection of early response to cyclophosphamide therapy. *Cancer Res*. 2001; 61:7747–7753. [PubMed: 11691788]
- Fischl B, Salat DH, Busa E, Albert M, Dieterich M, Haselgrove C, van der Kouwe A, Killiany R, Kennedy D, Klaveness S, Montillo A, Makris N, Rosen B, Dale AM. Whole brain segmentation: automated labeling of neuroanatomical structures in the human brain. *Neuron*. 2002; 33:341–355. [PubMed: 11832223]
- Garwood M, DelaBarre L. The return of the frequency sweep: Designing adiabatic pulses for contemporary NMR. *Journal of Magnetic Resonance*. 2001; 153:155–177. [PubMed: 11740891]
- Greve DN, Fischl B. Accurate and robust brain image alignment using boundary-based registration. *Neuroimage*. 2009; 48:63–72. [PubMed: 19573611]
- Hakumaki JM, Grohn OH, Tyynela K, Valonen P, Yla-Herttuala S, Kauppinen RA. Early gene therapy-induced apoptotic response in BT4C gliomas by magnetic resonance relaxation contrast T1 in the rotating frame. *Cancer Gene Ther*. 2002; 9:338–345. [PubMed: 11960284]
- Hakumaki JM, Poptani H, Sandmair AM, Yla-Herttuala S, Kauppinen RA. H-1 MRS detects polyunsaturated fatty acid accumulation during gene therapy of glioma: Implications for the in vivo detection of apoptosis. *Nature Medicine*. 1999; 5:1323–1327.
- Haris M, Singh A, Cai KJ, Davatzikos C, Trojanowski JQ, Melhem ER, Clark CM, Borthakur A. T1rho (T-1 rho) MR imaging in Alzheimer' disease and Parkinson's disease with and without dementia. *Journal of Neurology*. 2011; 258:380–385. [PubMed: 20924593]
- Hu BS, Conolly SM, Wright GA, Nishimura DG, Macovski A. PULSED SATURATION TRANSFER CONTRAST. *Magnetic Resonance in Medicine*. 1992; 26:231–240. [PubMed: 1325023]
- Hulvershorn J, Borthakur A, Bloy L, Gualtieri EE, Reddy R, Leigh JS, Elliott MA. T1rho contrast in functional magnetic resonance imaging. *Magn Reson Med*. 2005; 54:1155–1162. [PubMed: 16217783]
- Jokivarsi KT, Hiltunen Y, Grohn H, Tuunanen P, Grohn OH, Kauppinen RA. Estimation of the onset time of cerebral ischemia using T1rho and T2 MRI in rats. *Stroke*. 2010a; 41:2335–2340. [PubMed: 20814006]
- Jokivarsi KT, Hiltunen Y, Tuunanen PI, Kauppinen RA, Grohn OH. Correlating tissue outcome with quantitative multiparametric MRI of acute cerebral ischemia in rats. *J Cereb Blood Flow Metab*. 2010b; 30:415–427. [PubMed: 19904287]
- Jokivarsi KT, Niskanen JP, Michaeli S, Grohn HI, Garwood M, Kauppinen RA, Grohn OH. Quantitative assessment of water pools by T-1 rho and T-2 rho MRI in acute cerebral ischemia of the rat. *Journal of Cerebral Blood Flow and Metabolism*. 2009; 29:206–216. [PubMed: 18827834]
- Kettunen MI, Grohn OH, Silvennoinen MJ, Penttonen M, Kauppinen RA. Effects of intracellular pH blood, and tissue oxygen tension on T1rho relaxation in rat brain. *Magn Reson Med*. 2002; 48:470–477. [PubMed: 12210911]
- Kettunen MI, Sierra A, Narvainen MJ, Valonen PK, Yla-Herttuala S, Kauppinen RA, Grohn OH. Low spin-lock field T1 relaxation in the rotating frame as a sensitive MR imaging marker for gene therapy treatment response in rat glioma. *Radiology*. 2007; 243:796–803. [PubMed: 17517934]
- Kogan F, Singh A, Cai K, Haris M, Hariharan H, Reddy R. Investigation of chemical exchange at intermediate exchange rates using a combination of chemical exchange saturation transfer (CEST) and spin-locking methods (CESTRho). *Magn Reson Med*. 2012; 68:107–119. [PubMed: 22009759]
- Kupce E, Freeman R. Adiabatic Pulses for Wide-Band Inversion and Broad-Band Decoupling. *Journal of Magnetic Resonance Series A*. 1995; 115:273–276.

- Levitt MH, Freeman R, Frenkiel T. Broad-Band Heteronuclear Decoupling. *Journal of Magnetic Resonance*. 1982; 47:328–330.
- Liimatainen T, Sierra A, Hanson T, Sorce DJ, Ylae-Herttuala S, Garwood M, Michaeli S, Grohn O. Glioma cell density in a rat gene therapy model gauged by water relaxation rate along a fictitious magnetic field. *Magnetic Resonance in Medicine*. 2012; 67:269–277. [PubMed: 21721037]
- Liimatainen T, Sorce DJ, O'Connell R, Garwood M, Michaeli S. MRI Contrast From Relaxation Along a Fictitious Field (RAFF). *Magnetic Resonance in Medicine*. 2010; 64:983–994. [PubMed: 20740665]
- Mangia S, Liimatainen T, Garwood M, Michaeli S. Rotating frame relaxation during adiabatic pulses vs. conventional spin lock: simulations and experimental results at 4 T. *Magnetic Resonance Imaging*. 2009; 27:1074–1087. [PubMed: 19559559]
- Mellon EA, Beesam RS, Elliott MA, Reddy R. Mapping of cerebral oxidative metabolism with MRI. *Proc Natl Acad Sci U S A*. 2010; 107:11787–11792. [PubMed: 20547874]
- Michaeli S, Grohn H, Grohn O, Sorce DJ, Kauppinen R, Springer CS, Ugurbil K, Garwood M. Exchange-influenced T-2p contrast in human brain images measured with adiabatic radio frequency pulses. *Magnetic Resonance in Medicine*. 2005; 53:823–829. [PubMed: 15799068]
- Michaeli S, Oz G, Sorce DJ, Garwood M, Ugurbil K, Majestic S, Tuite P. Assessment of brain iron and neuronal integrity in patients with Parkinson's disease using novel MRI contrasts. *Movement Disorders*. 2007; 22:334–340. [PubMed: 17149719]
- Michaeli S, Sorce DJ, Garwood M. T-2 rho and T-1 rho adiabatic relaxations and contrasts. *Current Analytical Chemistry*. 2008; 4:8–25.
- Michaeli S, Sorce DJ, Idiyatullin D, Ugurbil K, Garwood M. Transverse relaxation in the rotating frame induced by chemical exchange. *Journal of Magnetic Resonance*. 2004; 169:293–299. [PubMed: 15261625]
- Michaeli S, Sorce DJ, Springer CS Jr, Ugurbil K, Garwood M. T1rho MRI contrast in the human brain: modulation of the longitudinal rotating frame relaxation shutter-speed during an adiabatic RF pulse. *J Magn Reson*. 2006; 181:135–147. [PubMed: 16675277]
- Park JY, Garwood M. Spin-Echo MRI Using  $\pi/2$  and  $\pi$  Hyperbolic Secant Pulses. *Magnetic Resonance in Medicine*. 2009; 61:175–187. [PubMed: 19097200]
- Pauly J, Leroux P, Nishimura D, Macovski A. PARAMETER RELATIONS FOR THE SHINNAR-LEROUX SELECTIVE EXCITATION PULSE DESIGN ALGORITHM. *Ieee Transactions on Medical Imaging*. 1991; 10:53–65. [PubMed: 18222800]
- Pipe JG. SPATIAL ENCODING AND RECONSTRUCTION IN MRI WITH QUADRATIC PHASE PROFILES. *Magnetic Resonance in Medicine*. 1995; 33:24–33. [PubMed: 7891532]
- Ramadan UA, Markkola AT, Halavaara J, Tanttu J, Hakkinen AM, Aronen HJ. On- and off-resonance spin-lock MR imaging of normal human brain at 0.1 T: possibilities to modify image contrast. *Magn Reson Imaging*. 1998; 16:1191–1199. [PubMed: 9858276]
- Redfield AG. On the Theory of Relaxation Processes. *Ibm Journal of Research and Development*. 1957; 1:19–31.
- Sepponen RE, Pohjonen JA, Sipponen JT, Tanttu JI. A METHOD FOR T1-RHO IMAGING. *Journal of Computer Assisted Tomography*. 1985; 9:1007–1011. [PubMed: 4056129]
- Sierra A, Michaeli S, Niskanen JP, Valonen PK, Grohn HI, Yla-Herttuala S, Garwood M, Grohn OH. Water spin dynamics during apoptotic cell death in glioma gene therapy probed by T-1 rho and T-2 rho. *Magnetic Resonance in Medicine*. 2008; 59:1311–1319. [PubMed: 18506797]
- Sorce DJ, Michaeli S, Garwood M. Relaxation during adiabatic radiofrequency pulses. *Current Analytical Chemistry*. 2007; 3:239–251.
- Sun Z, Bartha R. Enhanced diffusion weighting generated by selective adiabatic pulse trains. *Journal of Magnetic Resonance*. 2007; 188:35–40. [PubMed: 17600741]
- Tannus A, Garwood M. Adiabatic pulses. *Nmr in Biomedicine*. 1997; 10:423–434. [PubMed: 9542739]
- Valette J, Lethimonnier F, Lebon V. About the origins of NMR diffusion-weighting induced by frequency-swept pulses. *Journal of Magnetic Resonance*. 2010; 205:255–259. [PubMed: 20570538]

- van der Kouwe AJW, Benner T, Salat DH, Fischl B. Brain morphometry with multiecho MPRAGE. *Neuroimage*. 2008; 40:559–569. [PubMed: 18242102]
- Wangsness RK, Bloch F. The Dynamical Theory of Nuclear Induction. *Physical Review*. 1953; 89:728–739.
- Wheaton AJ, Borthakur A, Corbo M, Charagundla SR, Reddy R. Method for reduced SAR T-1p-weighted MRI. *Magnetic Resonance in Medicine*. 2004a; 51:1096–1102. [PubMed: 15170827]
- Wheaton AJ, Borthakur A, Kneeland JB, Regatte RR, Akella SVS, Reddy R. In vivo quantification of T-1 rho using a multislice spin-lock pulse sequence. *Magnetic Resonance in Medicine*. 2004b; 52:1453–1458. [PubMed: 15562469]
- Witschey WR 2nd, Borthakur A, Elliott MA, Mellon E, Niyogi S, Wallman DJ, Wang C, Reddy R. Artifacts in T1 rho-weighted imaging: compensation for B(1) and B(0) field imperfections. *J Magn Reson*. 2007; 186:75–85. [PubMed: 17291799]
- Zhou JY, Payen JF, Wilson DA, Traystman RJ, van Zijl PCM. Using the amide proton signals of intracellular proteins and peptides to detect pH effects in MRI. *Nature Medicine*. 2003; 9:1085–1090.

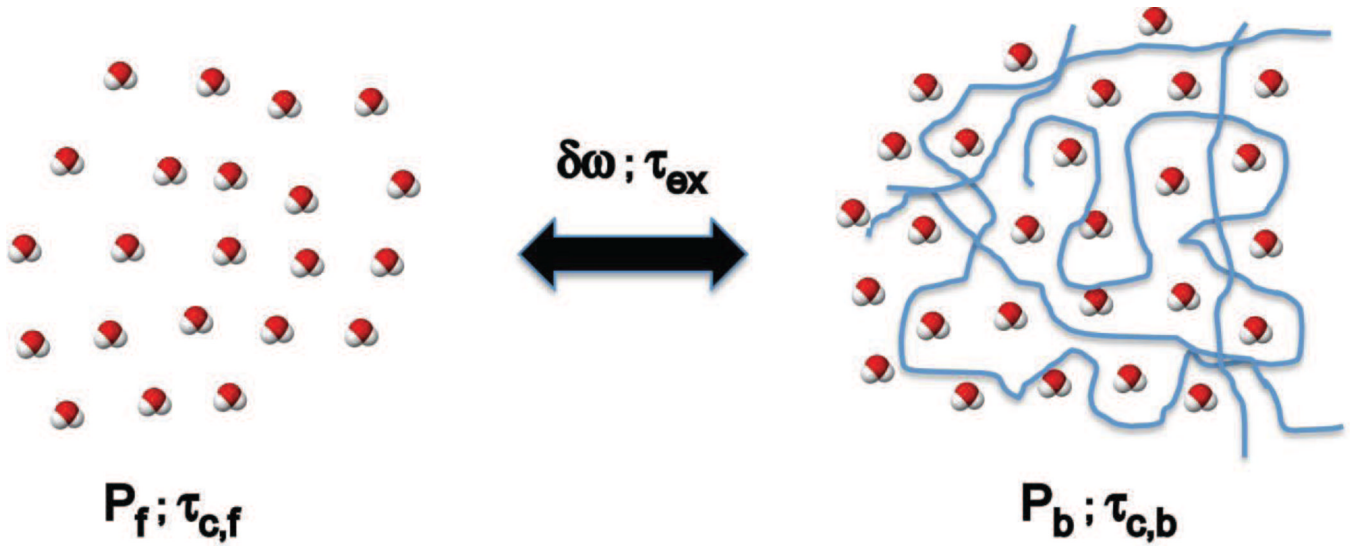
### Highlights

- Reduction of specific absorption rate (SAR) for T1 $\rho$  and T2  $\rho$  mapping
- Compensate B1 and B0 inhomogeneity and minimize image artifacts
- Slice selective T1 $\rho$  and T2  $\rho$  mapping
- Whole brain high resolution T1 $\rho$  and T2  $\rho$  mapping with reduced acquisition time
- Modeling, segmentation and statistical analysis of water dynamics in brain



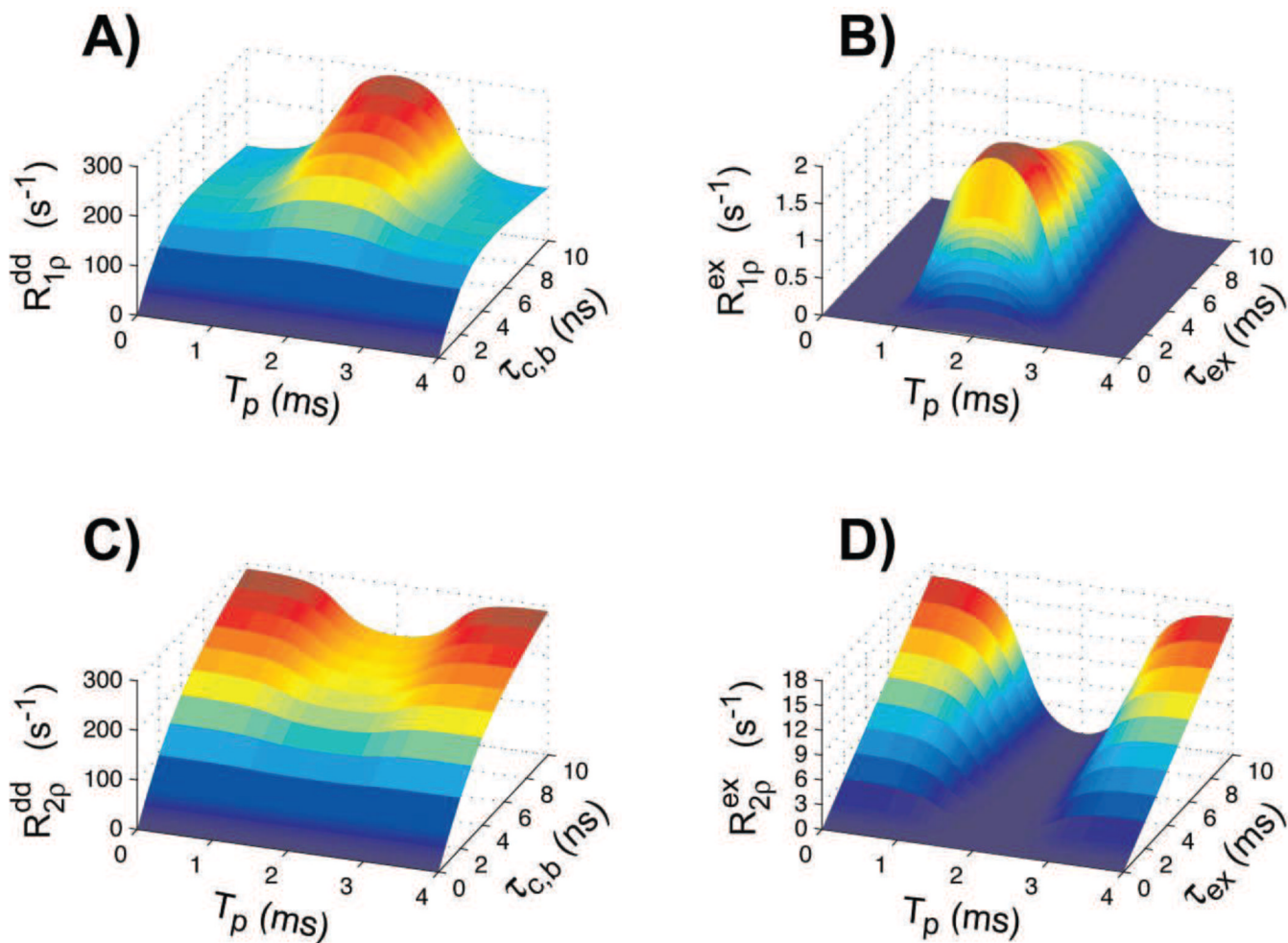
**Figure 1.**

Plots of GOIA-W(16,4) pulse: A)  $B_1$  amplitude modulation function; B) frequency sweep; C) gradient modulation; D) effective field; E) nutation angle; F) inverse of the adiabatic factor; G) slice profile at the isocenter; H) slice profile off-isocenter. A pulse duration of 4ms and bandwidth of 5kHz were assumed. In Fig.1D the rate of the nutation angle is also shown with the dashed line.

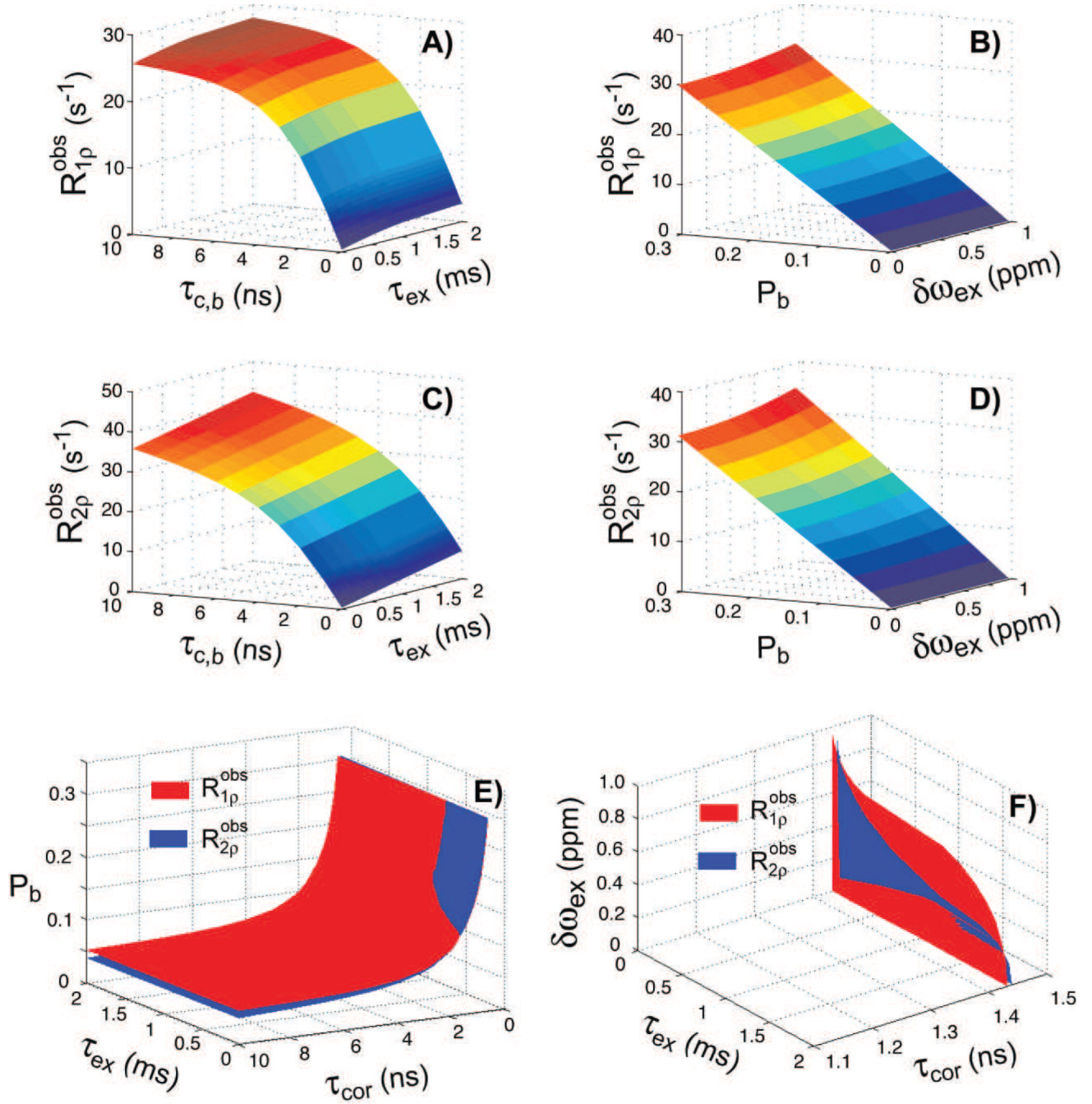


**Figure 2.**

Two site exchange (2SX) model depicting the pool of free water and pool of water bound to macromolecules. In each pool water molecules experience dipolar coupling relaxation governed by the correlation times  $\tau_c$  of each pool. The two pools are considered in an equilibrium anisochronous exchange determined by the exchange time  $\tau_{ex}$  and the chemical shift difference  $\delta\omega_{ex}$ . The model is specified by four independent parameters: correlation time  $\tau_{c,b}$  of bound water,  $\tau_{ex}$ ,  $\delta\omega_{ex}$  and bound water fraction  $P_b$  ( $P_f = 1 - P_b$  and  $\tau_{c,f} \approx 5$  ps). The fast exchange limit (FXL) it is assumed in-vivo  $\delta\omega_{ex}\tau_{ex} \ll 1$ .

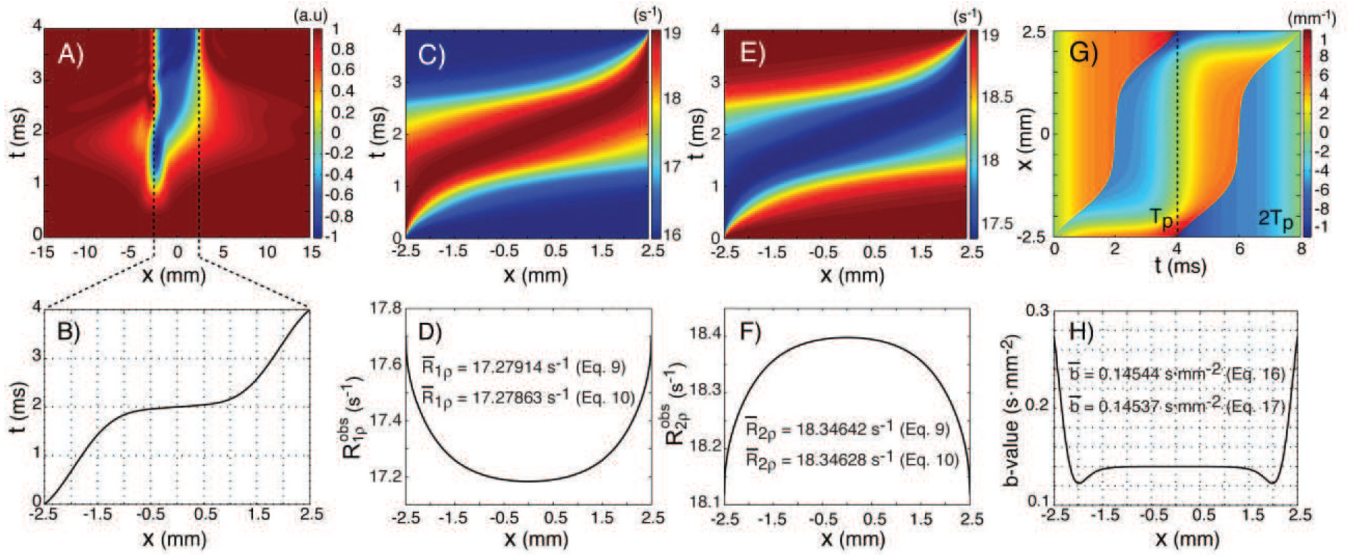


**Figure 3.** Simulations of longitudinal and transverse rotating frame relaxation rates for dipolar coupling (Eqs. 5) and exchange (Eqs. 6) interactions during GOIA-W(16,4) pulses of 4 ms duration, 5 kHz bandwidth and 0.382 kHz peak amplitude. For exchange interaction (Figs. 3B,D)  $P_b$  was fixed at 0.15 and  $\delta\omega_{ex}$  was assumed 0.8 ppm at 2.89T ( $\approx 100$  Hz). The  $B_0$  field was considered 2.89T.



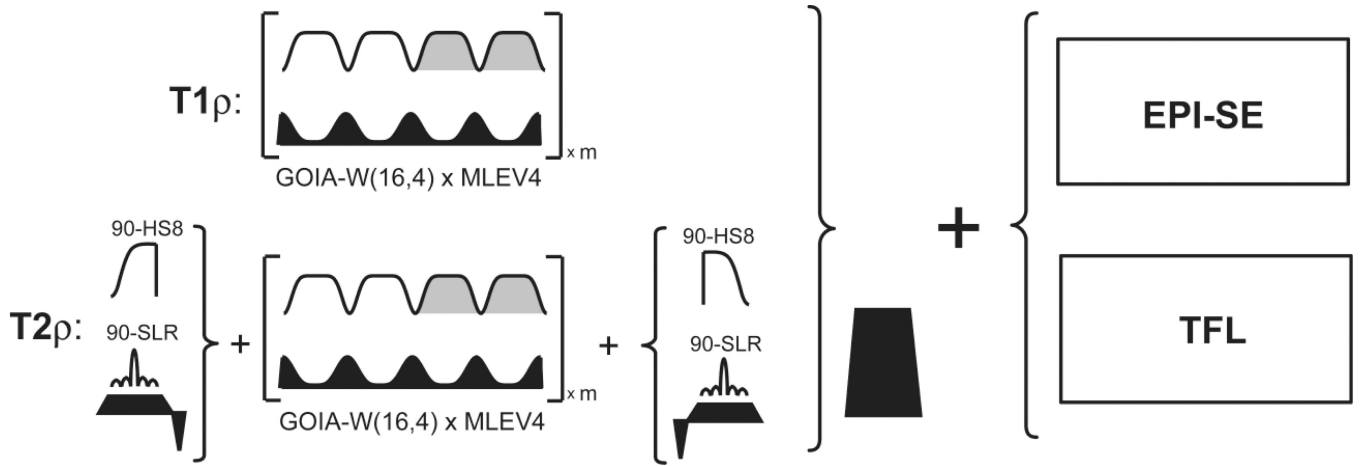
**Figure 4.** Simulations of observed longitudinal and transverse rotating frame relaxation rates for the 2SX/FXL model (Eqs. 7–9) during GOIA-W(16,4) pulses of 4 ms duration, 5 kHz bandwidth and 0.382 kHz peak amplitude. For simulations in Fig. 4(A,C)  $P_b$  was fixed at 0.15 and  $\delta\omega_{ex}$  was assumed 0.8 ppm at 2.89T ( $\approx 100$  Hz). For simulations in Fig. 4(B,D)  $\tau_{c,b} = 2$  ns and  $\tau_{ex} = 0.2$  ms. In Figs 4(E,F) the isosurfaces and their intersection through the parameter space are shown corresponding to  $T1p = 90$  ms and  $T2p = 85$  ms. Because of the 4 dimensional parameter space the isosurfaces are shown when one of the model parameters is fixed to a particular value. In Fig. 4E  $\delta\omega_{ex}$  was assumed 0.8 ppm, and Fig. 4F  $P_b$  was

assumed 0.15. The correlation time of free water was assumed  $\tau_{c,f} \approx 5$  ps. The  $B_0$  field was considered 2.89T.

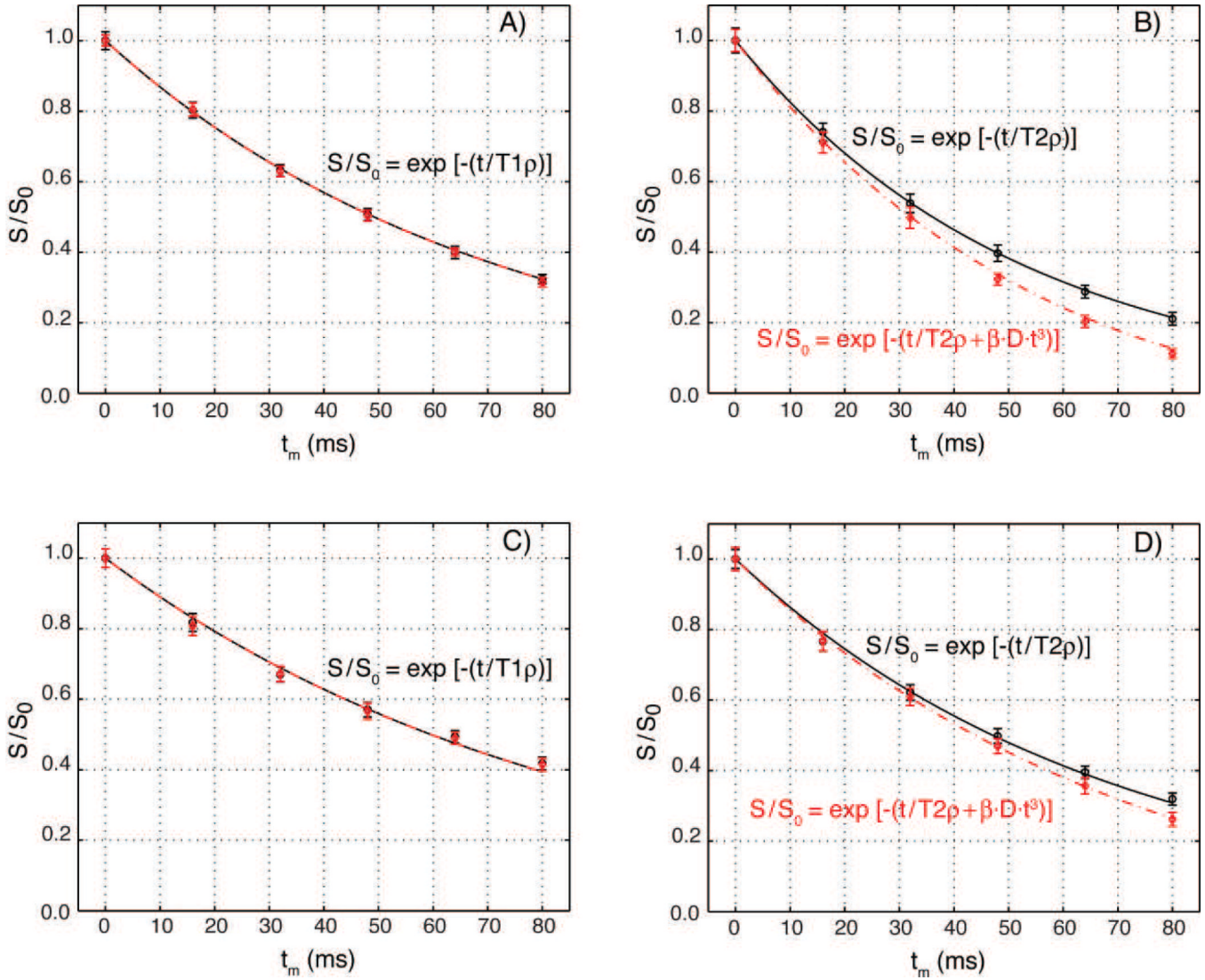


**Figure 5.**

Simulations of the magnetization inversion, rotating frame relaxation rates and b-values for the GOIA-W(16,4) pulse of 4ms and 5kHz. A) magnetization inversion during pulse across slice isochromats; B) isochromat inversion times; C) instantaneous and D) time averaged  $R_{1\rho}$  relaxation rate across slice isochromats; E) instantaneous and F) time averaged  $R_{2\rho}$  relaxation rate across slice isochromats; G) gradient moment for a pair of GOIA-W(16,4) pulses; H) b-values across slice isochromats for a pair of GOIA-W(16,4) pulses. For simulations of Figs 5C–F it was assumed that  $\tau_{c,b} = 2\text{ns}$ ,  $\tau_{ex} = 0.2 \text{ ms}$ ,  $\delta\omega_{ex} = 0.8 \text{ ppm}$ ,  $P_b = 0.15$ , and  $\tau_{c,f} \approx 5 \text{ ps}$ . The  $B_0$  field was considered 2.89T.

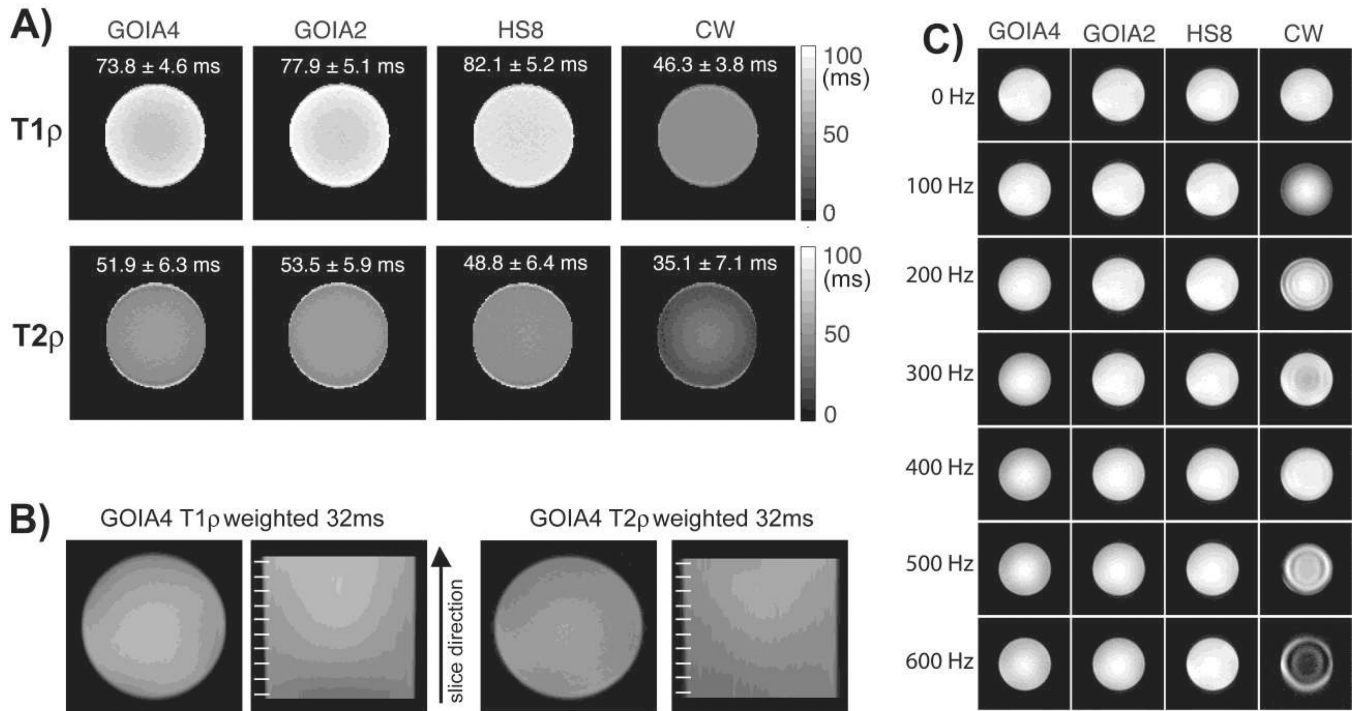


**Figure 6.** Pulse sequences for  $T1\rho$  and  $T2\rho$  mapping using GOIA-W(16,4) pulse trains. Turbo FLASH (TFL) or spin-echo EPI (EPI-SE) are used for image readout. GOIA-W(16,4) pulses are concatenated without gaps according to MLEV-4 phase cycle. For  $T2\rho$  mapping the GOIA-W(16,4) pulse train is preceded and followed by  $90^\circ$  pulses. For 2D slice selective  $T2\rho$  mapping  $90^\circ$  SLR pulses are used, while for 3D mapping  $90^\circ$  AHP-HS8 pulses are used. The gradient ramps of GOIA-W(16,4) pulses and the gradient of  $90^\circ$  SLR pulses are refocused. After  $T1\rho$  and  $T2\rho$  preparation a spoiler gradient is used to spoil any transverse magnetization that was not stored on the longitudinal direction.



**Figure 7.**

Diffusion effects in slice selective  $T1\rho$  and  $T2\rho$  experiments using GOIA-W(16,4) pulses of 4 ms duration and 5 kHz bandwidth. Relaxation curves were measured with a strong gradient (23.5 mT/m, 5 mm slice, red diamonds) and a very weak gradient (0.34 mT/m, 350 mm slab, black circles).  $T1\rho$  experiments in an agar phantom (Fig. 7A) and volunteers (Fig. 7C) show no difference in relaxation curves and can be fitted with the same relaxation time constant and an exponential decay ( $T1\rho = 71$  ms for agar, and  $T1\rho = 87$  ms for in-vivo).  $T2\rho$  experiments show differences between relaxation curves measured with strong and weak gradients in both agar (Fig. 7B) and volunteers (Fig. 7D). Signal decay with a weak gradient can be fitted with transverse relaxation time  $T2\rho = 52$  ms for agar and  $T2\rho = 68$  ms for volunteers. For strong gradient an additional diffusion term has to be included in the exponential signal decay. Data can be fitted with a coefficient  $\beta = 1.87 \cdot 10^6 \text{ mm}^{-2} \cdot \text{s}^{-2}$ , diffusion constant  $D = 2.1 \cdot 10^{-3} \text{ mm}^2 \cdot \text{s}^{-1}$  for agar and  $D = 0.8 \cdot 10^{-3} \text{ mm}^2 \cdot \text{s}^{-1}$  for volunteers, and the same transverse relaxation times used for the weak gradient. Diffusion constants were independently measured in the slice direction with a PGSE experiment. The difference between the weak and strong gradient transverse relaxation curves increases with diffusion constant. Error bars equal plus/minus two standard deviations.

**Figure 8.**

T1 $\rho$  and T2 $\rho$  maps in a uniform agar phantom. Fig. 8A shows maps obtained with: i) GOIA-W(16,4) pulses of 4 ms, 5 kHz bandwidth, 0.382 kHz peak amplitude (abbrev. GOIA4), ii) GOIA-W(16,3) pulses of 2 ms, 10 kHz bandwidth, 0.821 kHz peak amplitude (abbrev. GOIA2), iii) HS8 pulses of 4 ms, 5 kHz bandwidth, 0.886 kHz peak amplitude, iv) CW spin-lock with 0.886 kHz amplitude and  $B_1$  and  $B_0$  compensation. Fig. 8B shows multislice T1 $\rho$  and T2 $\rho$  weighted images acquired with the slice selective GOIA-W(16,4) preparation. The sagittal views shown in the slice direction have good uniformity and no slice cross-talking (slice position is indicated by the white lines on the right of each sagittal image). Fig. 8C shows the compensation of  $B_0$  inhomogeneity. The carrier frequency during T1 $\rho$  preparation was changed as noted on the left side. It can be seen that the CW spin-lock method shows artifacts due to  $B_0$  inhomogeneity despite using a  $B_0$  and  $B_1$  compensation scheme. Adiabatic methods show good compensation of  $B_0$  inhomogeneity over the entire range of offset frequencies.

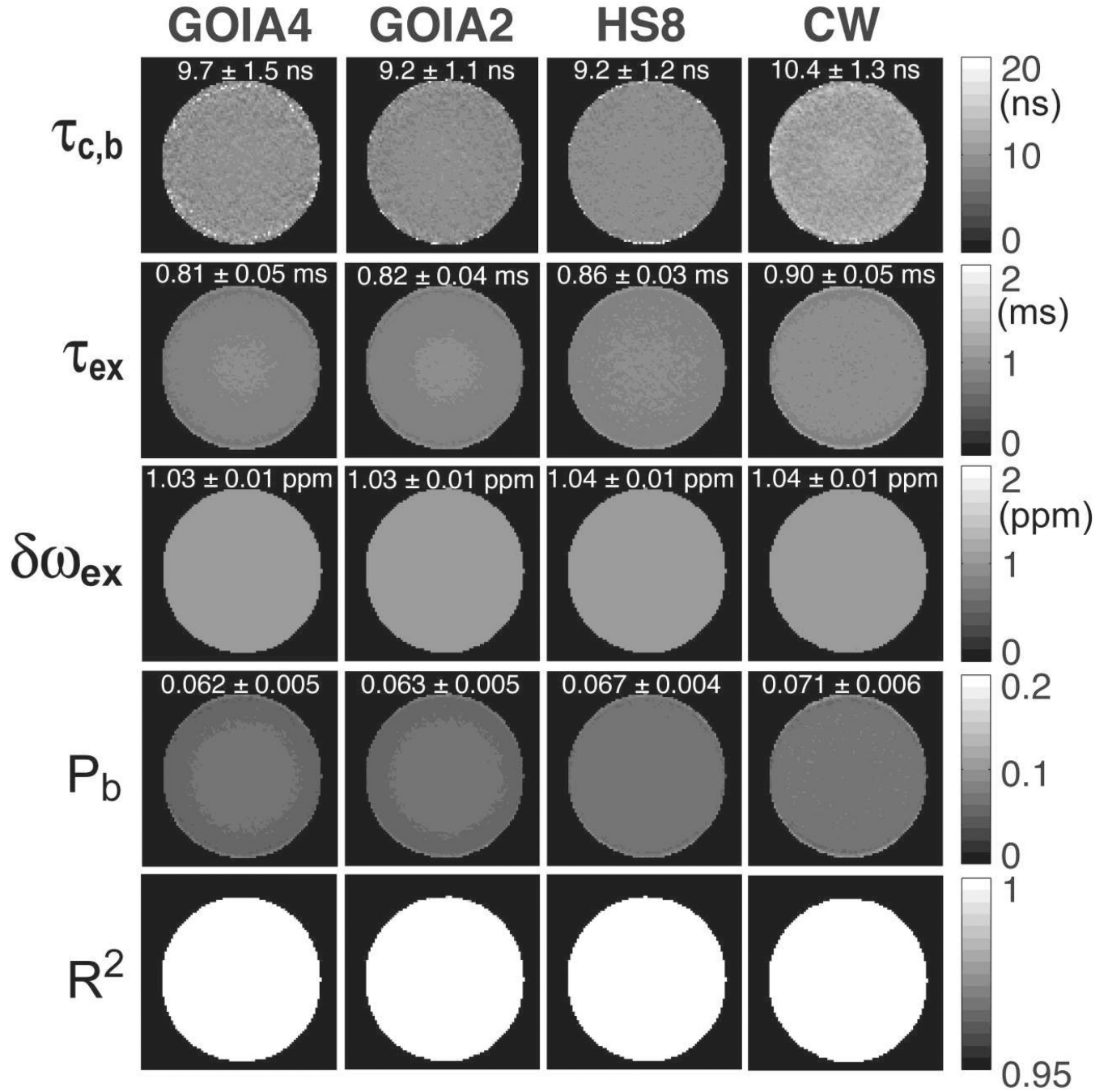


**Figure 9.**

Parametric maps of water molecular dynamic in the agar phantom obtained by fitting the 2SX/FXL model to experimental data from Fig. 8A. Uniform maps are obtained for all parameters. Mean values and standard deviation for each parameter and measurement are calculated. Mean values obtained with different methods are much closer than the relaxation times in Fig. 7A. The goodness of fit is indicated by the map of coefficient of determination  $R^2$  at the bottom.

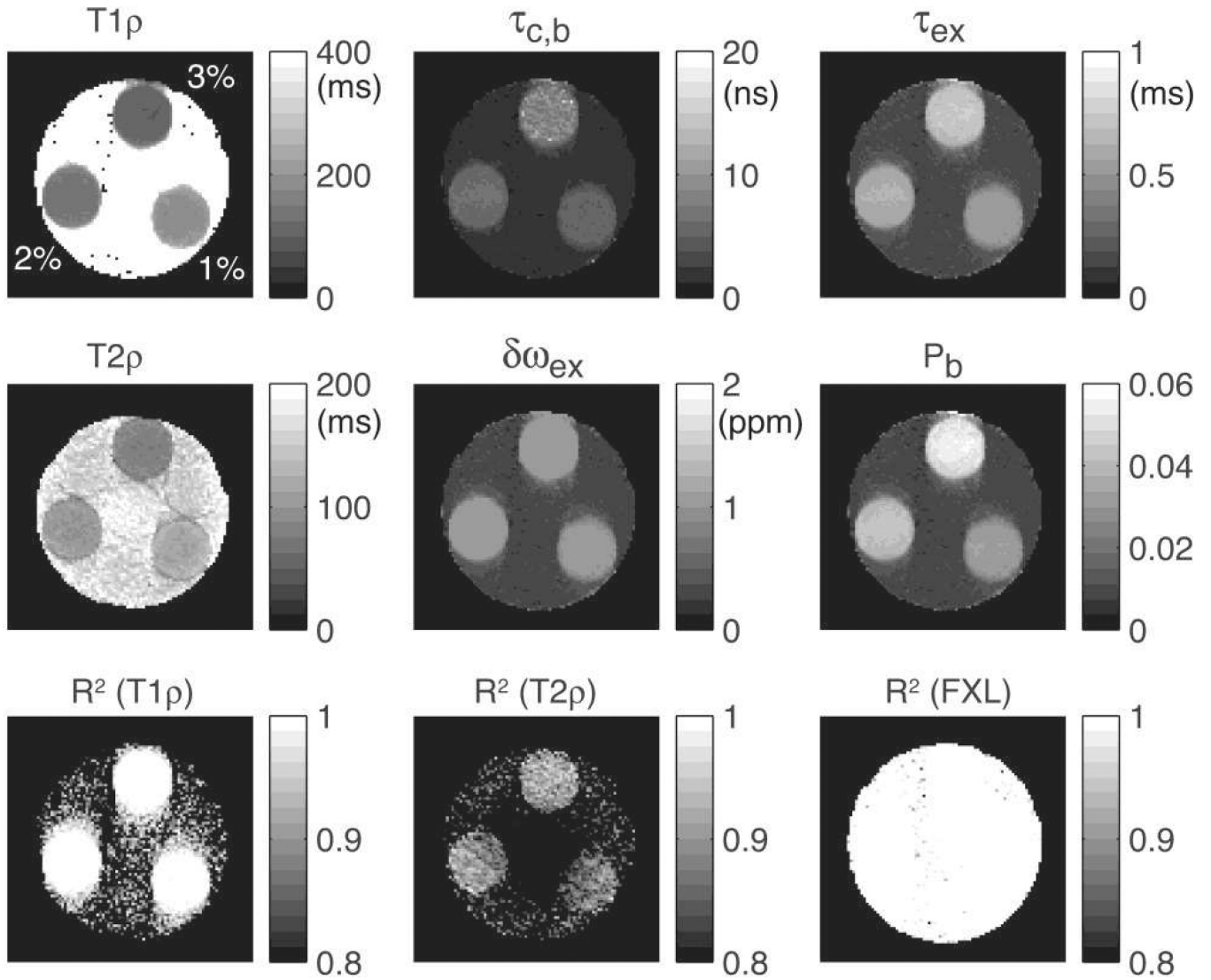


**Figure 10.**

Parametric maps of water molecular dynamics in a multi-compartment phantom containing three agar tubes prepared with 1%, 2% and 3% w/v. Good contrast can be seen between tubes in  $T1\rho$ ,  $T2\rho$ ,  $\tau_{c,b}$ ,  $\tau_{ex}$  and  $P_b$ . Chemical shift exchange frequency  $\delta\omega_{ex}$  is approximately 1 ppm in all tubes, showing, as expected, no dependency on agar concentration. Importantly, the map of water bound fraction  $P_b$  is able to distinguish a difference of 1% agar concentration. Goodness of fit is indicated by the coefficient of determination  $R^2$  showed in the bottom figures.

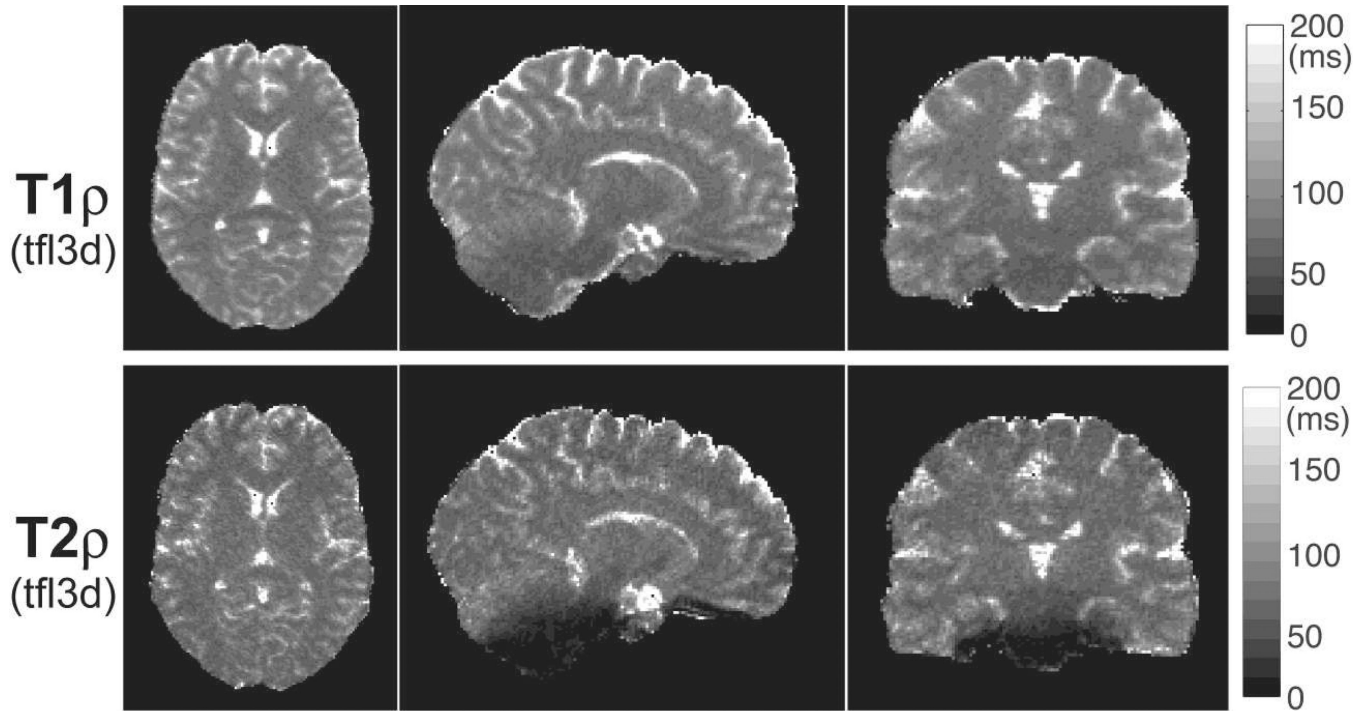


**Figure 11.**

3D  $T1\rho$  and  $T2\rho$  maps of the brain acquired in a volunteer. Five preparation periods of 0, 16, 32, 48 and 64 ms consisting of 0, 4, 8, 12 and 16 GOIA-W(16,4) pulses were acquired with 3D turbo FLASH at 1.33 mm isotropic resolution in 5:40 min.  $T1\rho$  map shows good uniformity in all three orthogonal cross-sections.  $T1\rho$  map shows good uniformity in all three orthogonal cross-sections.  $T2\rho$  map shows signal loss towards the base of the skull, predominantly in vermis and pons as seen in the sagittal and coronal views. Good contrast can be seen between gray and white matter, and subcortical structures.

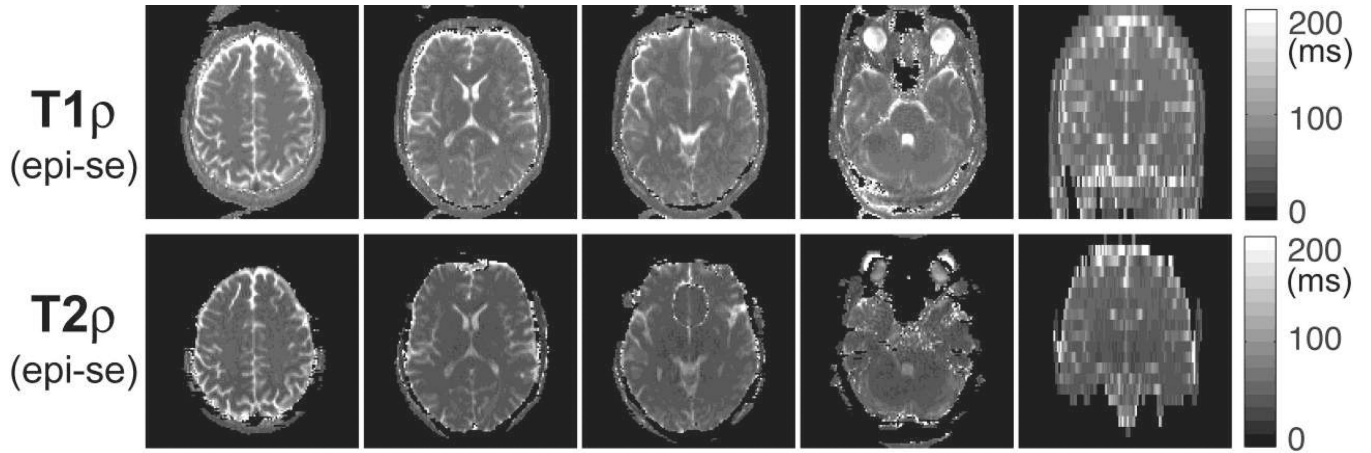


**Figure 12.**

2D slice selective T1 $\rho$  and T2 $\rho$  maps of the brain acquired in a volunteer. Six preparation periods of 0, 16, 32, 48, 64 and 80 ms consisting of 0, 4, 8, 12, 16 and 20 GOIA-W(16,4) pulses were acquired for 20 slices with 2D EPI-SE at  $2 \times 2 \times 5 \text{ mm}^3$  resolution in 1:17 min. T1 $\rho$  map shows good uniformity in all slices, while T2 $\rho$  map shows signal loss in slices at the base of the skull in regions with large susceptibility anisotropy. The coronal views on the right side indicate the prescription of slices and show no magnetization history between neighboring slices.

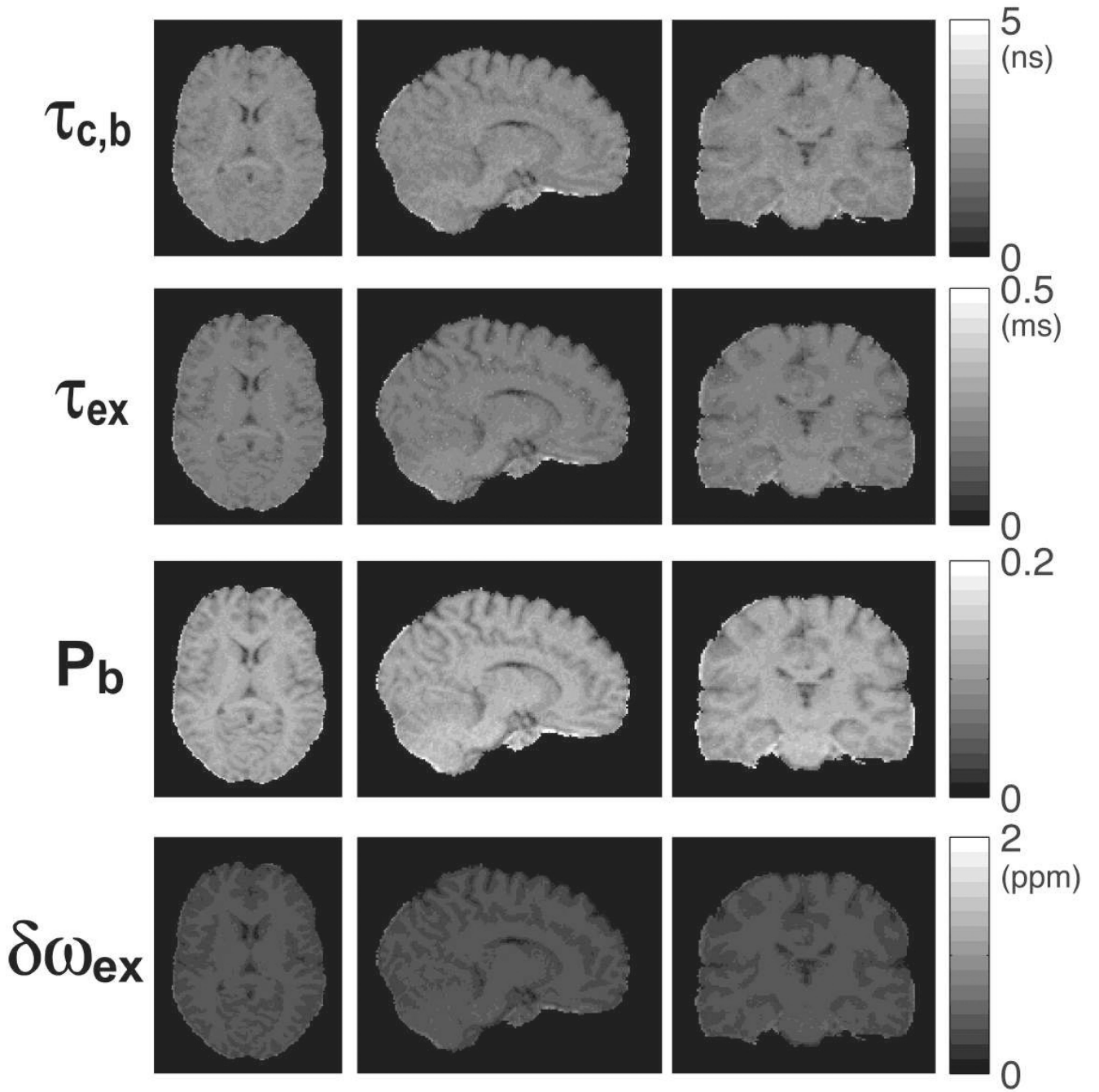


**Figure 13.**

3D parametric maps of water molecular dynamics in the brain of a human volunteer. The maps were obtained by fitting the 2SX/FXL model to rotating frame relaxation data from Fig. 11. Maps are uniform and without artifacts in all three orthogonal sections. Good contrast can be seen in all maps between gray and white matter, and subcortical structures.

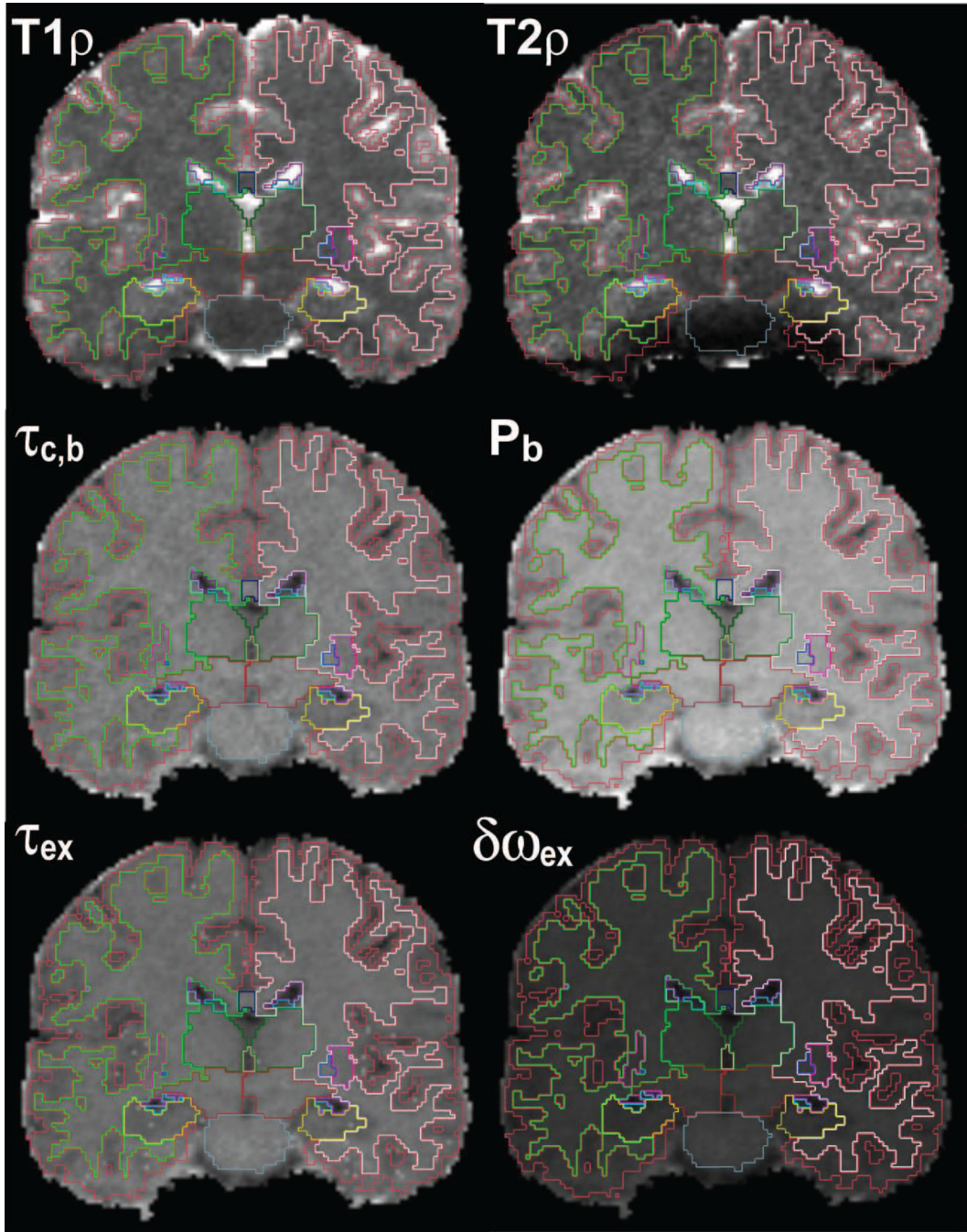


**Figure 14.** Segmentation of the T1 $\rho$ , T2 $\rho$  and water molecular dynamics maps. Cortical gray matter, white matter and subcortical structures were segmented on a high-resolution scan using Freesurfer 5.1. The high-resolution scan and segmentation were coregistered to the rotating frame relaxation data.

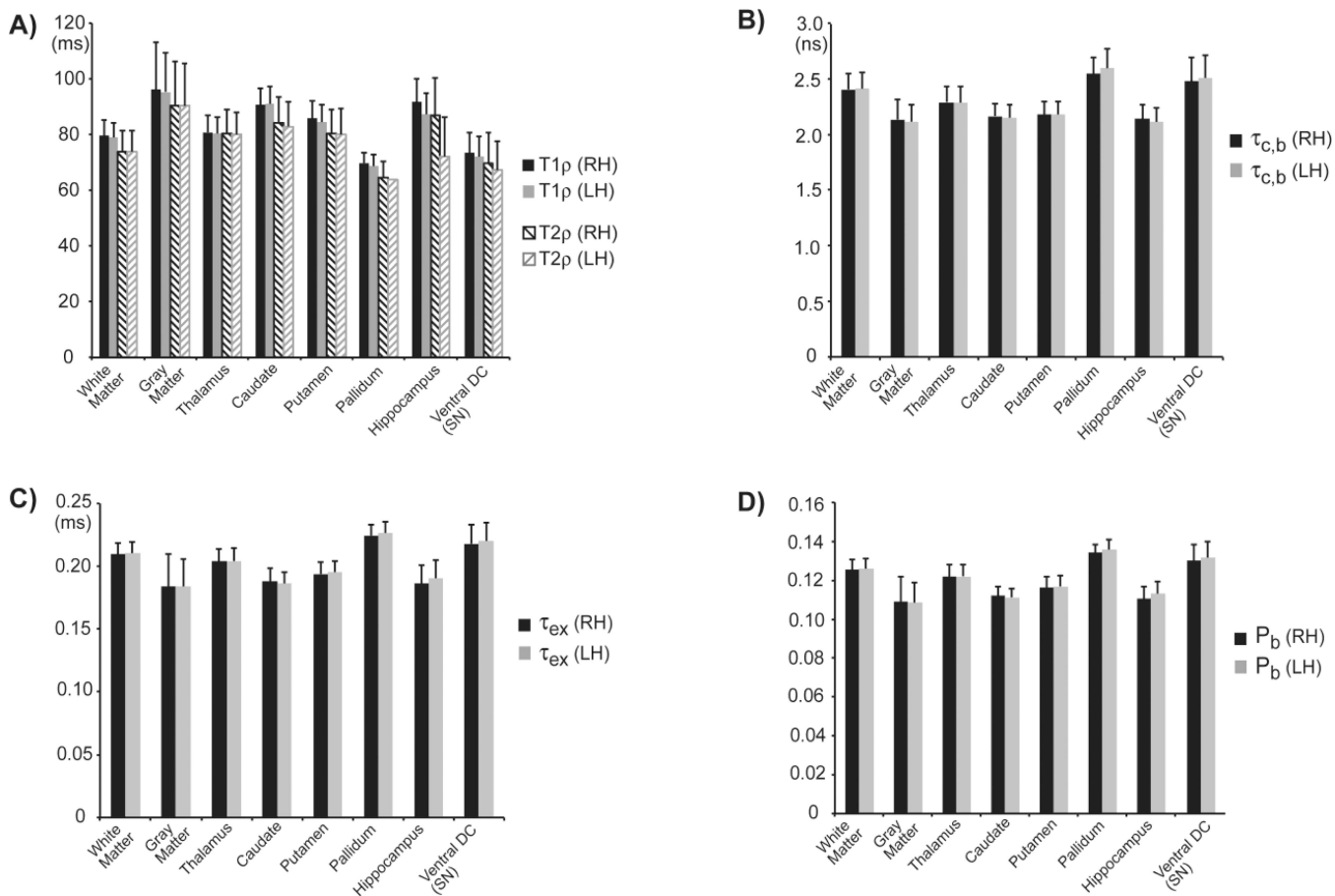


**Figure 15.** Statistical analysis of T1ρ, T2ρ and water molecular dynamics in eight ROIs segmented by Freesurfer in each hemisphere of the brain (RH - right hemisphere, LH - left hemisphere). Mean and standard deviation values are shown for all subjects. Only voxels with goodness of fit  $R^2 > 0.95$  were included. Edge voxels at the border of two ROIs were excluded.

**Table 1**

2SX/FXL modeling of agar T1 $\rho$  relaxation. Comparison of the model parameters obtained by fitting dispersion data or single relaxation decay curves. Dispersion data included rotating frame relaxation rates obtained at four different GOIA modulations as specified on the first row. Single fit data represented the relaxation decay curve measured with one GOIA modulation (4ms, GOIA-W(16,4),  $g_m = 0.9$ ,  $B_{1max} = 382$  Hz) different from the previous four. The model parameters were: correlation time constant  $\tau_{c,b}$ , exchange time constant  $\tau_{ex}$ , exchange chemical shift  $\delta\omega_{ex}$ , water bound fraction  $P_b$ .

GOIA	4ms, W(16,4), $g_m=0.6$	4ms, W(8,4), $g_m=0.8$	5ms, W(16,4), $g_m=0.9$	6ms, W(16,4), $g_m=0.9$
$B_{1max}$ (Hz)	640	510	305	255
T1 $\rho$ (ms)	90.04 $\pm$ 7.05	87.69 $\pm$ 7.40	80.38 $\pm$ 9.19	79.02 $\pm$ 8.59
Model parameters	$\tau_{c,b}$ (ns)	$\tau_{ex}$ (ms)	$\delta\omega_{ex}$ (ppm)	$P_b$
Dispersion fit	8.403 $\pm$ 0.346	0.815 $\pm$ 0.044	0.997 $\pm$ 0.003	0.065 $\pm$ 0.003
Single fit	9.429 $\pm$ 2.301	0.827 $\pm$ 0.063	1.034 $\pm$ 0.006	0.063 $\pm$ 0.006

Table 2

Mean and standard deviation values for longitudinal T1 $\rho$  relaxation, transverse T2 $\rho$  relaxation, correlation time constant  $\tau_{c,b}$ , exchange time constant  $\tau_{ex}$ , exchange chemical shift  $\delta\omega_{ex}$ , water bound fraction  $P_b$ . Values are calculated in eight ROIs segmented by Freesurfer 5.1 on high-resolution 3D anatomical scans and coregistered to the 3D rotating frame relaxation maps acquired in the brains of five human volunteers. Only voxels with a coefficient of determination  $R^2 > 0.95$  were used for statistical analysis. Voxels at the boundary of ROIs were also excluded. RH – right hemisphere, LH – left hemisphere, Ventral DC – ventral diencephalon, SN – substantia nigra.

Brain ROI	T1 $\rho$ (ms)	T2 $\rho$ (ms)	$\tau_{c,b}$ (ms)	$\tau_{ex}$ (ms)	$\delta\omega_{ex}$ (ppm)	$P_b$	
White Matter	RH	79.5 $\pm$ 5.5	73.9 $\pm$ 7.5	2.40 $\pm$ 0.15	0.21 $\pm$ 0.01	0.42 $\pm$ 0.02	0.125 $\pm$ 0.005
	LH	79.0 $\pm$ 5.4	73.9 $\pm$ 7.4	2.41 $\pm$ 0.15	0.21 $\pm$ 0.01	0.42 $\pm$ 0.02	0.126 $\pm$ 0.005
Gray Matter	RH	96.1 $\pm$ 16.9	90.4 $\pm$ 15.8	2.13 $\pm$ 0.18	0.18 $\pm$ 0.03	0.36 $\pm$ 0.04	0.109 $\pm$ 0.013
	LH	95.3 $\pm$ 13.9	90.3 $\pm$ 15.1	2.11 $\pm$ 0.15	0.18 $\pm$ 0.02	0.36 $\pm$ 0.03	0.108 $\pm$ 0.010
Thalamus	RH	80.8 $\pm$ 6.2	80.5 $\pm$ 8.6	2.29 $\pm$ 0.14	0.20 $\pm$ 0.01	0.41 $\pm$ 0.02	0.122 $\pm$ 0.006
	LH	80.3 $\pm$ 6.0	80.0 $\pm$ 8.1	2.29 $\pm$ 0.15	0.20 $\pm$ 0.01	0.41 $\pm$ 0.02	0.122 $\pm$ 0.006
Caudate	RH	90.7 $\pm$ 5.9	84.2 $\pm$ 9.5	2.16 $\pm$ 0.11	0.19 $\pm$ 0.01	0.37 $\pm$ 0.02	0.112 $\pm$ 0.005
	LH	90.9 $\pm$ 6.3	82.9 $\pm$ 8.9	2.15 $\pm$ 0.12	0.19 $\pm$ 0.01	0.37 $\pm$ 0.02	0.111 $\pm$ 0.005
Putamen	RH	85.8 $\pm$ 6.5	80.4 $\pm$ 8.6	2.18 $\pm$ 0.11	0.19 $\pm$ 0.01	0.39 $\pm$ 0.02	0.116 $\pm$ 0.006
	LH	84.5 $\pm$ 6.2	80.0 $\pm$ 9.2	2.18 $\pm$ 0.11	0.20 $\pm$ 0.01	0.39 $\pm$ 0.02	0.117 $\pm$ 0.005
Pallidum	RH	69.8 $\pm$ 3.7	64.5 $\pm$ 5.8	2.55 $\pm$ 0.15	0.22 $\pm$ 0.01	0.45 $\pm$ 0.01	0.134 $\pm$ 0.004
	LH	68.7 $\pm$ 3.9	64.0 $\pm$ 5.3	2.59 $\pm$ 0.17	0.23 $\pm$ 0.01	0.45 $\pm$ 0.02	0.136 $\pm$ 0.005
Hippocampus	RH	91.8 $\pm$ 8.2	86.8 $\pm$ 13.7	2.14 $\pm$ 0.13	0.19 $\pm$ 0.01	0.37 $\pm$ 0.02	0.111 $\pm$ 0.006
	LH	87.2 $\pm$ 7.7	72.2 $\pm$ 14.1	2.11 $\pm$ 0.13	0.19 $\pm$ 0.01	0.38 $\pm$ 0.02	0.113 $\pm$ 0.006
Ventral DC (SN)	RH	73.4 $\pm$ 7.4	69.9 $\pm$ 10.7	2.48 $\pm$ 0.21	0.22 $\pm$ 0.01	0.43 $\pm$ 0.03	0.130 $\pm$ 0.008
	LH	72.1 $\pm$ 7.3	67.2 $\pm$ 10.4	2.50 $\pm$ 0.21	0.22 $\pm$ 0.01	0.44 $\pm$ 0.03	0.132 $\pm$ 0.008